Microglia reactivity entails microtubule remodeling from acentrosomal to centrosomal arrays

Running Title: *Microtubules in microglia reactivity*

Authors: Maria Rosito[1,2]*, Caterina Sanchini[1,2]*, Giorgio Gosti[3], Manuela Moreno[2], Simone De Panfilis[1], Maria Giubettini[4], Doriana Debellis[5], Federico Catalano[5], Giovanna Peruzzi[1], Roberto Marotta[5], Alessia Indrieri[6,7], Elvira De Leonibus[6,8], Maria Egle De Stefano[9], Davide Ragozzino[2,10], Giancarlo Ruocco[1,3], Silvia Di Angelantonio[1,2]*‡, Francesca Bartolini[11]*‡

Affiliations:

[1]Center for Life Nano- & Neuro- Science, Istituto Italiano di Tecnologia; Rome, 00161, Italy.

[2]Department of Physiology and Pharmacology, Sapienza University; Rome, 00185, Italy

[3]Department of Physics, Sapienza University; Rome, 00185, Italy.

[4]Crestoptics S.p.A.; Rome, 00165, Italy

[5]Electron Microscopy Facility, Istituto Italiano di Tecnologia; Genova 16163, Italy.

[6]Telethon Institute of Genetics and Medicine; Pozzuoli, 80078 Italy.

[7]Institute for Genetic and Biomedical Research, National Research Council; Milan, 20090, Italy.

[8]Institute of Biochemistry and Cellular Biology, National Research Council; Rome, 00015, Italy.

[9]Department of Biology and Biotechnologies "Charles Darwin", Sapienza University; Rome, 00185, Italy.

[10]Santa Lucia Foundation (IRCCS Fondazione Santa Lucia); Rome, 00179, Italy

[11]Department of Pathology and Cell Biology, Columbia University Medical Center; New York, NY 10032

*These authors contributed equally to this work. ‡Corresponding authors. Email: silvia.diangelantonio@uniroma1.it; fb2131@cumc.columbia.edu

Abstract: Microglia reactivity entails a large-scale remodeling of cellular geometry, but the role of the microtubule cytoskeleton during these changes remains unexplored. Here we show that

reactive proinflammatory microglia provide a heretofore unique example of microtubule reorganization from a non-centrosomal array of parallel and stable microtubules to a radial array of more dynamic microtubules. While in the homeostatic state microglia nucleate microtubules at Golgi outposts, proinflammatory signaling induces recruitment of nucleating material nearby the centrosome and inhibition of centrosomal maturation enhances NLRP3 inflammasome activation and secretion of IL-1β. Our results demonstrate that a hallmark of microglia reactivity is a striking remodeling of the microtubule cytoskeleton and suggest that pericentrosomal microtubule nucleation may serve as a distinct marker of microglia activation as well as a novel target to modulate cytokine-mediated inflammatory responses in chronic disease and tissue injury.

INTRODUCTION

Microglia are the brain's primary innate immune cells. In their homeostatic state in the healthy brain, they exhibit a ramified morphology and continuously patrol the local environment via extension and retraction of highly motile processes [1] that act to clear cellular debris, reshape synapses, and provide neurotrophic factors [2–8]. However, when activated by neuronal inflammation and injury, and in neurodegenerative disorders, microglia exhibit dramatically altered gene expression and morphology, displaying an amoeboid shape [9–11]. In this pro-inflammatory state, reactive microglia exhibit phagocytic activities that can promote tissue remodeling and if over-activated, are widely thought to contribute to brain damage and neurodegeneration [2,12].

In eukaryotes, changes in cellular symmetry are associated with massive reorganization of both the actin and microtubule (MT) cytoskeletons. While actin and actin-based motor proteins are required for breaking the symmetry in most cells, specification of neuronal polarity depends on MTs and MT associated proteins [13]. Early studies suggested changes in MT spatial organization and stability also with microglia activation [14]. Despite these observations, however, only remodeling of the actin cytoskeleton has been extensively studied in microglia, and the role of the MT cytoskeleton in breaking cellular polarity during the transition from an homeostatic to a reactive state has not been explored.

MTs are intrinsically polarized polymers composed of α/β tubulin heterodimers arranged in a head to tail fashion [15]. They are characterized by a fast growing plus end and a slow growing minus end that in non-neuronal cells is often attached to the centrosome, which acts as the MT

organizing center (MTOC). Directional transport is enabled by the structural polarity of MTs, which is recognized by motor proteins that drive transport to either the minus end (dynein) or plus end (most kinesins) (for reviews see [16, 17]). MTs are generally highly dynamic structures constantly undergoing stochastic transitions from polymerization to depolymerization (catastrophe events) and vice-versa (rescue events), with the two dynamic states exhibiting characteristic rates of growth or shrinkage [18]. When stabilized, MTs resist disassembly and become substrates of tubulin modifying enzymes that add molecular moieties on either the α- or β-tubulin subunit. The combinatorial nature of these modifications provides a "tubulin code" which controls a variety of functions, including organelle transport and the mechanical properties of the MT lattice (for reviews see [19–21]).

MT orientation, density, and post-translational modifications all respond and contribute to breaking cellular symmetry [22,23]. Establishment of cell polarity can be achieved through centrosome repositioning or by the formation of non-radial MT arrays, in which MTs are not preferentially nucleated at the centrosome [24–26]. During this transition, the centrosome typically loses its maximal MT nucleating activity while intracellular membranes or self-organizing assemblies of MT nucleating material distant from the centrosome serve as non-centrosomal MTOCs with members of the calmodulin-regulated spectrin-associated protein (CAMSAP) family often capping and stabilizing released free MT minus ends [27,28]. The local stabilization of non-centrosomal MTs and relocation of the MTOCs away from the centrosome and the cell center establish asymmetric MT arrays that are critical to cell differentiation.

We hypothesized that rearrangement of the MT cytoskeleton might be required for the morphological changes that guide microglia transition from surveilling/homeostatic to reactive states. Here we show that proinflammatory microglia engage a unique example of MT transition from a non-centrosomal array of parallel and stable MTs in the homeostatic state to a radial array of more dynamic MTs in which all MT minus ends are anchored to a pericentrosomal region. We further find that in the homeostatic state, Golgi outposts are sites of non-centrosomal MT nucleation, and that a pro-inflammatory challenge leads to the recruitment of pericentriolar material (PCM) to the centrosome. To investigate the regulatory role of this transition we inhibited the master modulator of MTOC assembly Polo-like kinase 4 (PLK4) and found that failure to mature *de novo* formed pericentrosomal MTOCs increases the number of small diameter extracellular vesicles (EVs) and selectively enhances IL-1β secretion. Our results unveil the unique

89 rearrangement of the MT cytoskeleton in proinflammatory microglia and indicate that
90 pericentriolar material re-localization and assembly can alone limit the release of IL-1β.
91
92 **MATERIALS AND METHODS**
93 Primary murine microglia culture and treatment
94 Primary cortical glial cells were prepared from 0- to 2-d-old mice as previously described [29].
95 Briefly, cerebral cortices were chopped and digested in 30 U/ml papain for 40 min at 37 °C
96 followed by gentle trituration. The dissociated cells were washed, suspended in Dulbecco′s
97 Modified Eagle′s Medium (DMEM, Sigma-Aldrich by Merck KGaA, Darmstadt, Germany) with
98 10% FBS (Gibco by Life Technologies, Carlsbad, CA, USA) and 2 mM L-glutamine and plated
99 at a density of 9–10 x 105 in 175 cm^2 cell culture flasks. At confluence (10 –12 DIV), glial cells
100 were shaken for 2 h at 37 °C to detach and collect microglial cells. These procedures gave an
101 almost pure (<1% astrocyte contamination) microglial cell population. Microglia cells were plated
102 at a density of 7x103/cm^2 (to prevent cell contact activation) in astrocytes conditioned medium
103 /DMEM 2,5% FBS (1:1). The day after plating microglia cells were treated for 48 h with IFNγ (20
104 ng/ml) and LPS (100 ng/ml) or with IL-4 (20 ng/ml) to obtain the pro-inflammatory or anti-
105 inflammatory phenotype, respectively. To disassemble MTs, homeostatic microglia were treated
106 with 2 µM nocodazole (Sigma-Aldrich) added to the culture medium for 1 h at 37 °C. Samples
107 were then kept on ice and washed 5x times with ice-cold medium. MTs were allowed to regrow in
108 conditioned medium without nocodazole for 15 min and 120 min at 37 °C. Right before fixation,
109 free tubulin was rapidly extracted using a MT-preserving extraction buffer (60 mM PIPES, 25 mM
110 HEPES, 10 mM EGTA, 2 mM MgCl2, 0.1% saponin, pH 6.9, [30]) for 20 sec at 37 °C. Cells were
111 subsequently fixed with methanol at -20 °C for 4 min and processed for immunofluorescence
112 staining. To stabilize MTs, microglia cells were treated for 24 h with 1 nM and 5 nM Taxol (Sigma-
113 Aldrich) alone or together with IFNγ (20 ng/ml) and LPS (100 ng/ml). To inhibit PLK4, microglia
114 cells were pre-treated with 125 nM Centrinone (Tocris Bioscience, Bristol, UK) for 12 h prior to
115 stimulation for 48 h with IFNγ (20 ng/ml) and LPS (100 ng/ml).
116
117 Immunofluorescence staining on fixed cells
118 Methanol fixation at -20 °C was elected for preserving an intact MT cytoskeleton: culture medium
119 was removed and cells were fixed with pre-cooled 100% methanol at -20°C for 4 min prior to re-
120 hydration with Phosphate-buffered saline (PBS, 0.01 M phosphate buffer, 0.0027 M potassium

121 chloride and 0.137 M sodium chloride, pH 7.4, at 25 °C, Sigma-Aldrich) for at least 30 min at RT
122 To preserve membrane associated components, cells were fixed with 4% paraformaldehyde
123 (PFA)/PBS for 15 min at RT and then washed with PBS. When PFA fixed, cells were
124 permeabilized with 0.1% Triton X-100/PBS for 1 to 3 min. After 2 washes in PBS, cells were
125 blocked with 3% bovine serum albumin (BSA, Sigma-Aldrich) in PBS for 1 h at RT Primary
126 antibodies (Rabbit Camsap1L1, Novus Biologicals, Englewood, CO, USA, 1:200; rabbit γ-tubulin,
127 Invitrogen, Waltham, MA, USA, 1: 5000; mouse γ tubulin, Sigma-Aldrich, 1:1000; rat Tyrosinated
128 tubulin YL 1/2, Merck-Millipore, 1:1000; mouse Acetylated tubulin clone 6-11B-1, Sigma-
129 Aldrich, 1:1000; mouse α-tubulin clone DM1A, Sigma-Aldrich, 1:500; rabbit Detyrosinated α-
130 tubulin, Merck-Millipore, 1:1000; mouse EB1, BD Biosciences, San Jose, CA, USA 1:100; rabbit
131 Pericentrin, Abcam, Cambridge, UK, 1:1500; mouse Centrin3, Abnova, Taipei City, Taiwan,
132 1:100; mouse GM130, BD Biosciences, 1:600; rabbit IBA-1, FujiFilm Wako, Richmond, VA,
133 1:300; Atto 488 Phalloidin, Sigma-Aldrich, 1:50) were incubated in 1.5% BSA in PBS for 2 h
134 (RT) or overnight (+4°C). Cells were then extensively washed and stained with fluorophore-
135 conjugated secondary antibodies in PBS (Alexa Fluor 488 goat anti-mouse, 488 goat anti-rat, 488
136 goat anti-rabbit, 594 goat anti-mouse, 647 goat anti-rabbit, Invitrogen; CF 594 goat anti-rat,
137 Sigma-Aldrich; 1:500) and Hoechst (Sigma-Aldrich) for nuclei visualization for 1 h at RT prior to
138 wash and mounting using Ibidi Mounting Medium.
139
140 MT dynamics assay
141 For live fluorescence imaging to measure MT dynamics, cells were incubated with 100 nM SiR-
142 Tubulin (SpiroChrome, Stein-am-Rhein, Switzerland) at 37 °C for 30 min and washed with
143 conditioned medium prior to visualization to improve signal to noise ratio. 10 µM Verapamil was
144 added to inhibit efflux pumps and improve labeling. Live wide-field fluorescence imaging of
145 SiRTub-labeled MTs was performed on a Olympus IX73 microscope, LDI laser source and
146 CoolSNAP Myo camera, 4.54 µm pixels (Photometrics, Tucson, AZ, USA) with a built-in
147 incubator, maintaining the temperature at 37 °C during recordings. Acquisitions were performed
148 for 4 min (1 frame/4 sec) with a UPLSXAPO100x/1.45 oil objective and then analyzed with
149 ImageJ software (see Image preparation and analysis).
150
151 Animals

152 All procedures performed using laboratory animals were in accordance with the Italian and
153 European guidelines and were approved by the Italian Ministry of Health in accordance with the
154 guidelines on the ethical use of animals from the European Communities Council Directive of
155 September 20, 2010 (2010/63/UE). All efforts were made to minimize suffering and number of
156 animals used. Mice were housed in standard cages in a group of a maximum of 5 animals, with
157 light–dark cycles of 12 h at 22±2 °C. Wild type C57BL-6 male and pregnant mice were purchased
158 from Charles River and pups (P0-P2) were used to obtain primary glial cultures. Cx3cr1$^{gfp/gfp}$ male
159 mice were purchased from The Jackson Laboratory company (B6.129P2(Cg)-Cx3cr1tm1Litt/J);
160 the colony was established in our animal facility, and progenitors were bred to C57BL6J to obtain
161 cx3cr1$^{gfp/+}$ mice as we previously reported [31].
162
163 Intravitreal injection and EIU
164 Adult C57BL6/J mice were intravitreally injected with sterile PBS (vehicle) or 5 ng/µl LPS from
165 E. Coli (O55:B5, Sigma Aldrich). Intravitreal injection of LPS has been previously reported as a
166 model of endotoxin induced uveitis (EIU) activating microglia in the retina [32–36]. Animals were
167 anaesthetized with 100 mg/kg methadomidine and 0.25 mg/kg ketamine. Pupils were dilated using
168 1% tropicamide and 2.5% phenylephrine (Chauvin, Essex, UK) and a small guide hole was made
169 under the limbus with a 30G needle. The eye was gently massaged with a cotton swab to remove
170 a portion of the vitreous to avoid a post-injection reflux of vitreous and/or drug solution. Then, 1
171 µl of vehicle or LPS solution was intravitreally injected through the initial hole using a 34G
172 Hamilton syringe.
173
174 Immunofluorescence staining on retinal tissue
175 Cx3cr1$^{gfp/+}$ control mice were sacrificed at P70. CTRL (sham) and LPS intravitreally injected adult
176 C57BL6/J mice were sacrificed 20 h after the injection procedure. Eyes were removed and kept in
177 4% PFA solution overnight. Eyes were then cryoprotected in 30% sucrose and, after precipitation,
178 frozen in isopentane prior to storage at -80 °C. Frozen eyes were cut in 50-µm-thick sections with
179 a Leica cryostat and processed for immunofluorescence staining as published [37]. Briefly, slices
180 were immersed for 30 min in a boiling 1 mM EDTA solution (pH = 8.0) for antigen retrieval, then
181 incubated with blocking solution (0.1% Triton X-100, 3% BSA and 0.05% Tween-20 in PBS) for
182 1 h at RT. Sections were incubated with primary antibodies (Iba1, FujiFilm Wako, 1:500; γ-
183 tubulin, clone GTU-88, Sigma-Aldrich, 1:500; GM130, BD bioscience, 1:500) in diluted blocking

184 solution overnight at 4 °C and 1 h at RT with fluorophore-conjugated secondary antibodies (Alexa
185 Fluor 488 goat anti-rabbit, 594 goat anti-mouse) and Hoechst for nuclei visualization. The sections
186 were mounted with anti-fade mounting medium (Invitrogen).
187
188 Confocal Spinning Disk and Structured Illumination (SIM) microscopy
189 For fluorescence imaging of fixed samples, images were collected with spinning disk confocal
190 microscopy on a Nikon Eclipse Ti equipped with X-Light V2 spinning disk (CrestOptics, Rome,
191 Italy), combined with a VCS (Video Confocal Super resolution) module (CrestOptics) based on
192 structured illumination, and a LDI laser source (89 North, Williston, VT, USA) and Prime BSI
193 Scientific CMOS (sCMOS) camera, 6.5 µm pixels (Photometrics) or a CoolSNAP Myo camera,
194 4.54 µm pixels (Photometrics), with a 10x/0.25 NA Plan E air objective, 40x/0.75 PlanApo l air
195 objective, a 60x/1.4 PlanApo l oil objective and a 100x/1.45 Plan E oil objective. The used Z step
196 size was 0.2 µm for spinning disk and 0.1 µm for VCS. In order to achieve super-resolution, raw
197 data obtained by the VCS module have been processed with a modified version of the joint
198 Richardson-Lucy (jRL) algorithm [38–40], where the out of focus contribution of the signal has been
199 explicitly added in the image formation model used in the jRL algorithm, and evaluated as a pixel-
200 wise linear "scaled subtraction" [41] of the raw signal. Retinal sections images were acquired on an
201 Olympus IX73 microscope equipped with X-Light V3 spinning disk (CrestOptics), LDI laser
202 source and a Prime BSI Scientific CMOS (sCMOS), 6.5 µm pixels (Photometrics) with a
203 UPLSXAPO100x/1.45 oil objective. All the images were acquired by using Metamorph software
204 version 7.10.2. (Molecular Devices, Wokingham, UK) and then analyzed with ImageJ software
205 (see Image preparation and analysis).
206
207 Image preparation and analysis
208 For image preparation, we used the open-source software ImageJ [42] for adjustments of levels and
209 contrast, maximum intensity projections, and thresholding signals for fluorescence intensity
210 analysis.
211 *Radial profile analysis.* For tyrosinated α-tubulin, CAMSAP2 and γ-tubulin distribution analysis,
212 microglia cells were fixed in methanol at -20 °C for 4 min or PFA 4% for 15 min and then stained
213 with an anti-tyrosinated tubulin, CAMSAP2 or γ-tubulin antibody according to the
214 immunofluorescence protocol, and Hoechst for nuclei visualization. Images obtained by confocal
215 microscopy were analyzed with ImageJ to identify the coordinates of the center of the nucleus in

216 each cell and to generate single-cell masks based on the morphology of each cell. A Python script
217 (see Supplementals) was written to apply an Otsu threshold to the images [43] and to perform a radial
218 scanning of fluorescence values, starting from the center of the nucleus of each cell, with a
219 resolution of 0.065 µm. Maximum value radial profile was defined as the maximum fluorescence
220 intensity (a.u.) for each concentric circle with an increasing distance from the nucleus center. For
221 each analyzed microglia cell the radial profile of the maximum value of fluorescence intensity
222 (a.u.) was computed and plotted. Plots were smoothed with a resolution of 0.5 µm. All data points
223 were exported into a Microsoft Excel 2010 compatible format. In CAMSAP2 analysis, only
224 cytoplasmic staining was analyzed. Curve fit was performed using a single exponential decay
225 function on GraphPad Prism 9.0 (Y=(Y0 - Plateau)*exp(-K*X) + Plateau).
226 MT dynamics analysis. Analysis of MT dynamics was performed by tracing the lengths of the
227 MTs via the "freehand line" tracing tool in ImageJ. Changes in length between successive frames
228 were exported into an Excel sheet to determine the growth, shortening and pause events for each
229 MT. Only changes >0.5 µm were considered growth or shortening events [44,45]. MT dynamics
230 parameters were defined as follows: growth/shrinkage rate: distance (µm) covered in growth or
231 shrinkage per second; % pause/growth/shrinkage: number of frames in pause/growth/shrinkage
232 divided total number of frames X 100; catastrophe/rescue frequency (sec-1): number of
233 catastrophe or rescue events divided by the product of the time of analysis and the percentage of
234 growth or shrinkage; MT dynamicity: the sum of total length in growth and shortening divided by
235 the time of analysis.
236 *In vitro cell morphology analysis.* Cell morphology analysis was performed using a quantitative
237 measurement of cell area; cell solidity is expressed as the ratio between cell area and convex area.
238 Measurements were obtained with the Particle Analysis tool and images were processed with
239 ImageJ.
240 *Extracellular vesicle analysis.* For the statistical analysis of EV blebbing from the surface of
241 microglia, 20 microglia cells per sample, collected in four different areas of the support, were
242 randomly selected and scanned to count and measure the visualized vesicles. The ImageJ software
243 was used to count and measure the vesicle major axis.
244 *Immunofluorescence signal quantification.* For immunofluorescence signal quantification, cells
245 were selected based on the representative morphology: ramified for homeostatic, ameboid for pro-
246 inflammatory and bipolar for anti-inflammatory states. Detyr/Tyr tubulin ratio and Acetyl/Tyr
247 tubulin ratio were calculated from the mean gray values of the respective immunofluorescence

signals, obtained from sum slices z-projections of 15 confocal planes after background subtraction (calculated as mean gray value of three circle background areas). EB1 anterograde or retrograde comets were defined from the EB1 fluorescence signal gradient from single plane images, measured with the "plot profile" tool of ImageJ. For Golgi stacks analysis, GM130 maximum intensity z-projection immunofluorescence images were uniformly thresholded on ImageJ by setting the same minimum values ('Default' threshold) to identify single Golgi stacks; a single Golgi stack was defined as a non-round object (roundness < 0.9) with a major axis length > 0.5 µm. For GM130- γ-tubulin co-staining analysis, GM130 and tubulin signals from max intensity z-projections were uniformly processed among different images increasing the 'brightness' and 'contrast' parameters by the same percentage. γ-tubulin signal over cell area was calculated as percentage of cell area covered by γ tubulin signal; γ-tubulin signal threshold was uniformly applied on MetaMorph analysis software by setting the same minimum values to all images. Two or more distinct γ-tubulin^{+} puncta were identified by counting the peaks of fluorescence intensity on a linescan drawn through the centroid of each puncta using the free-hand tool on ImageJ; The Find Peaks ImageJ plugin was used to identify the peaks by setting the minimum peak amplitude value at 100 grey values. Puncta were identified in a 132x132 pixels pericentriolar region after uniformly thresholding max intensity z-projections ('Default' threshold); integrated density was calculated in ImageJ as mean gray value*thresholded area. Pericentrin and Centrin-3- γ-tubulin co-localization analysis was performed by defining Pericentrin and Centrin-3^{+} puncta as described above for γ-tubulin^{+} puncta.

Retinal microglia cell skeleton analysis. Morphology of microglia cells in retinal sections was analyzed on max intensity z-projections; only entirely visible cells inside the acquisition field were analyzed; cells were isolated and then skeletonized on binary images, using the dedicated ImageJ plug-in; branches, endpoints and junction number was calculated from the skeletonized image.

<u>Real time PCR</u>

RNA was extracted from microglia cells with the Quick RNA MiniPrep (Zymo Research, Freiburg, DE) and retrotranscribed with iScript Reverse Transcription Supermix for Real-time PCR (RT-PCR) (Bio-Rad, Hercules, CA, USA). RT-PCR was carried out using Sybr Green (Bio-Rad) according to the manufacturer's instructions. The PCR protocol consisted of 40 cycles of denaturation at 95 ◦C for 30 s and annealing/extension at 60 ◦C for 30 s. For quantification, the comparative Threshold Cycle (Ct) method was used. The Ct values from each gene were

280 normalized to the Ct value of GAPDH in the same RNA samples. Relative quantification was
281 performed using the 2−ΔΔCt method [46] and expressed as fold change in arbitrary values. The
282 primers were used as below: GAPDH forward TCGTCCCGTAGACAAAATGG; GAPDH
283 reverse TTGAGGTCAATGAAGGGGTC; Ym1 forward CAGGTCTGGCAATTCTTCTGAA;
284 Ym1 reverse GTCTTGCTCATGTGTGTAAGTGA; Fizz1 forward
285 CCAATCCAGCTAACTATCCCTCC; Fizz1 reverse ACCCAGTAGCAGTCATCCCA; Tnfα
286 forward GTGGAACTGGCAGAAGAG; Tnfα reverse CCATAGAACTGATGAGAGG; IL1β
287 forward GCAACTGTTCCTGAACTCAACT; IL1 β reverse ATCTTTTGGGGTCCGTCAACT;
288 iNOS forward ACATCGACCCGTCCACAGTAT; iNOS reverse
289 CAGAGGGGTAGGCTTGTCTC.
290
291 SEM analysis
292 Samples were fixed in a solution of 1.5% Glutaraldehyde in 0.1 M Cacodylate buffer for 2 h at RT
293 and post-fixed in 1% osmium tetroxide in Milli q (MQ) H2O for 2 h. After several washes in MQ
294 H2O, the samples were subsequently dehydrated in rising concentrations of ethanol in H2O
295 solutions (from 30% to 100%), 1:1 ethanol:hexamethyldisilazane (HMDS, Sigma-Aldrich) and
296 100% HMDS and dried overnight in air. Finally, the samples were sputtered with a 10 nm gold
297 layer and analyzed using a JEOL JSM-6490LA Scanning Electron Microscope (SEM) operating
298 at 10 KV of accelerating voltage.
299
300 Western blot
301 Cells were lysed in Laemmli sample buffer and boiled at 95 °C for 5 min. Proteins were separated
302 by 4-12% Bis-Tris gel (Invitrogen) and transferred onto nitrocellulose membrane. After blocking
303 in 5% milk/TBS (Tris 20 mM, NaCl 150 mM), membranes were incubated with primary antibodies
304 at 4 °C overnight prior to 1 h incubation with secondary antibodies and signal detected using a
305 commercial chemiluminescent assay (Immun-Star WesternC Kit; Bio-Rad). Image acquisition was
306 performed with ChemiDoc MP imaging system (Bio-Rad) and densitometric analysis was
307 performed with Quantity One software (Bio-Rad).
308
309 Cell cycle assay
310 Microglia cells were collected by following trypsin treatment. Cells were rinsed twice with
311 phosphate buffered saline (PBS pH 7.4) and collected by centrifugation. Pellets were resuspended

312 in ice cold 70% ethanol and stored at 4 °C for 1 h. Cells were collected by centrifugation, rinsed
313 twice in PBS and resuspended in 20 µg/ml propidium iodide (PI) in PBS with 50 µg/ml RNase A
314 for a minimum of 30 min. After PI incubation, Flow cytometry analysis of DNA content was
315 performed as reported and analyzed using a BD LSRFortessa (BD Biosciences). The percentage
316 of cells in different phases of the cell cycle was determined using the FlowJo V10.7.1 computer
317 software (TreeStar, Ashland, OR, USA). At least 10.000 events for each sample were acquired.
318

319 Statistical analysis

320 The n number for each experiment and details of statistical analyses are described in the figure
321 legends or main text. Data are reported as mean ± SEM; when not normally distributed, data are
322 reported as median ± interquartile range. Origin 6 and GraphPad Prism 9 software were used for
323 statistical analysis. Normality tests were performed with Prism 9 and nonparametric tests were
324 used when appropriate. Significant differences are indicated in the figures by * $p < 0.05$, ** $p < 0.01$,
325 *** $p < 0.001$. Notable non-significant differences are indicated in the figures by ns.
326

327 **RESULTS**

328 **Homeostatic, pro-inflammatory and anti-inflammatory primary microglia differ in MT**
329 **distribution, stability and dynamic behaviour**

330 To investigate the organization of the MT cytoskeleton in homeostatic and reactive microglia, we
331 used primary mouse microglia cultures in which the presence of ramified cells was maintained by
332 growth factors secreted by astrocytes [47]. With this approach we prepared a nearly pure population
333 of primary microglia comprised by 99% of Iba1 positive cells. To steer microglia towards different
334 reactivity states such as a pro-inflammatory or an alternatively polarized microglia state (defined
335 as anti-inflammatory), cells were challenged with either LPS-IFNγ (100 ng/ml – 20 ng/ml 48 h for
336 pro-inflammatory) or IL-4 (20 ng/ml, 48 h for anti-inflammatory), and measured for the expression
337 of their signature activation genes (Figure S1A). As revealed by Iba1 staining (Figure S1B),
338 polarized microglia underwent dramatic morphological changes. We classified cell morphology
339 as ramified (≥3 ramifications), ameboid or bipolar based on number of cellular processes, cell area,
340 and solidity, a measure of cell shape complexity (Figure S1B-D). Analysis of morphology
341 distribution under homeostatic, pro-inflammatory and anti-inflammatory conditions revealed that
342 ramified cells were enriched in untreated microglia (35 ± 3%) (Figure S1B and S1D), while
343 ameboid cells represented a large majority after pro-inflammatory stimulation (82 ± 3%) (Figure

344 S1B and S1D). Conversely, when cells were challenged with an anti-inflammatory stimulus,
345 microglia mostly acquired a unipolar or bipolar rod-shape morphology (54 ± 3%) characterized by
346 the presence of a lamellipodium and a trailing edge, or uropod (Figure S1B and S1D). To further
347 detail the structural changes associated with reactive microglia states *via* single-cell analyses, we
348 chose to select for comparison only the most representative morphology of each *in vitro* phenotype
349 (ramified for homeostatic, amoeboid for pro-inflammatory and bipolar for anti-inflammatory
350 microglia).

351 We employed scanning electron microscopy (SEM) and confocal microscopy to identify
352 defined ultrastructural elements typical of each functional state (Figure S1E). Homeostatic
353 microglia exhibited many branched processes extending outward from the cell body and multiple
354 filopodia-like structures (Figure S1E) that were also positive for phalloidin staining (Figure S1H).
355 Upon pro-inflammatory challenge, microglia retracted most of their processes and acquired a
356 flattened and round morphology (Figure S1E and S1H). SEM imaging further revealed that pro-
357 inflammatory microglia displayed numerous tethered extracellular vesicles (EVs) blebbing from
358 the cell surface (Figure S1F). Analysis of EV diameter showed a bell-shaped distribution of size,
359 ranging from 250 to 650 nm (Figure S1G), consistent with microglia-shedded microvesicles [48].
360 Anti-inflammatory microglia were characterized by extensive membrane ruffling at both uropod
361 and leading edge, which appeared as sheet-like structures on the dorsal cell surface (Figure S1E
362 and S1H).

363 We began to analyze the MT cytoskeleton in each microglia functional state by
364 immunofluorescence staining of tyrosinated α-tubulin (Tyr tub), a bulk tubulin marker labeling
365 the entire MT network. MTs appeared to be packed in a parallel fashion in all the cellular branches
366 extending from the cell body in both homeostatic and anti-inflammatory microglia (Figure 1A).
367 However, MTs distributed radially from a perinuclear region in pro-inflammatory microglia (Fig.
368 1A). Radial profiling of Tyr tub fluorescence intensity (Figure 1A), a measure of the distribution
369 of tubulin signal that is independent of cell shape, confirmed that MT staining was uniformly
370 distributed along the entire cell profile in homeostatic and anti-inflammatory microglia (Figure
371 1B), while in pro-inflammatory cells, Tyr tub signal rapidly decayed at increasing distances from
372 a perinuclear region (Figure 1B; exponential decay constant $k_{pro\text{-}inf} = 0.046 \pm 0.001$; $k_{homeo} = 0.013$
373 ± 0.002; $k_{anti\text{-}inf} = 0.015 \pm 0.002$).

374 To evaluate whether microglial MTs differed in stability according to their reactive state,
375 we analyzed levels and distribution of detyrosinated and acetylated tubulins, two independent

376 tubulin post-translational modifications (PTMs) associated with MT longevity [19,49].
377 Semiquantitative immunofluorescence analyses revealed that homeostatic cells had the highest
378 level of both detyrosinated (Figure 1C, left) and acetylated (Figure 1C, right) tubulin compared to
379 pro-inflammatory or anti-inflammatory microglia (De-tyr/Tyr tub: 0.30± 0.03; 0.04 ± 0.01; 0.03 ±
380 0.01, Acetyl/Tyr tub: 1.02 ± 0.05; 0.69 ± 0.04; 0.72 ± 0.04 in homeostatic, pro-inflammatory and
381 anti-inflammatory microglia respectively; Figure 1D), suggesting that homeostatic microglia
382 display more stable MTs.

383 We quantified the behavior of SiR-Tubulin labeled MTs [50] in shallow peripheral sections
384 of the cell to measure MT plus end dynamics using time lapse wide field fluorescence microcopy
385 (Figure 1E). No change was observed among the three different microglia states in rescue
386 frequency (frequency of transitions from shrinkage to growth) or the fraction of time spent in
387 pausing or shrinkage. However, while pro-inflammatory and anti-inflammatory microglia MTs
388 exhibited a moderate yet significative drop in catastrophe frequency (frequency of transitions from
389 growth to shrinkage), they also significantly enhanced their growth rates and acquired a nearly 2.5
390 fold increase in rates of shrinkage, resulting in an overall net rise in MT dynamicity compared to
391 MTs of homeostatic cells (0.06 ± 0.01; 0.08 ± 0.01; 0.09 ± 0.01 in homeostatic, pro-inflammatory
392 and anti-inflammatory microglia respectively; Figure 1F, Table 1, Movies S1-3). In summary, and
393 consistent with our analysis of tubulin PTMs, these data suggest that microglia acquisition of pro-
394 and anti-inflammatory phenotypes is characterized by loss of MT stability and a marked increase
395 in MT dynamics.
396

397 **Homeostatic, pro-inflammatory and anti-inflammatory microglia differ in MT orientation**

398 In most dividing and motile cells, the centrosome is responsible for MT nucleation and
399 anchoring, leading to the formation of radial MT arrays in which all MT minus ends are attached
400 to the centrosome, while MT plus ends extend towards the cell periphery. In contrast, in most
401 differentiated, stationary and axially polarized cells, MTs are more stable and organized in non-
402 centrosomal arrays that are non-radially anchored at the centrosome [27].

403 We hypothesized that in microglia, the transition from the homeostatic phenotype to a
404 migrating reactive state would be paralleled by prominent changes in cell polarity driven by the
405 remodeling of MT anchoring and orientation. To test this, we analyzed the localization and
406 expression of endogenous MT plus end (EB1) and minus end (CAMSAP2) markers in
407 homeostatic, pro-inflammatory and anti-inflammatory microglia cells that had been selected

408 according to their most representative morphology (Figure 2 and S2). While EB1 is a widely
409 adopted marker of actively growing MT plus ends (comets), members of the CAMSAP family
410 regulate the formation and stability of non-centrosomal MT arrays by capping free MT minus ends
411 [24,51]. Confocal immunofluorescence analysis showed that in pro-inflammatory and anti-
412 inflammatory microglia, EB1 decorated most free MT ends (Tyr tub stained) (pro-inflammatory,
413 88%; anti-inflammatory, 82%) that extended towards the cell periphery (Figure 2A), confirming
414 the existence of a prominent pool of dynamic MTs arranged radially with their minus ends attached
415 to a perinuclear region of the cell. EB1 comets were also clearly visible at MT ends in homeostatic
416 microglia although to a lesser extent (homeostatic 63% of MTs $p < 0.001$, see Figure S2A for
417 contingency analysis). Western blot analysis of whole cell lysates showed that total EB1 protein
418 levels did not change in reactive microglia compared to homeostatic cells (Figure S2B and S7).
419 However, a detailed measurement of fluorescence intensity gradients of EB1 positive comets with
420 respect to the location of the cell nucleus (Figure 2B, arrows) identified distinct MT polarity
421 patterns, with anterograde and retrograde orientation. Specifically, a population of retrograde
422 comets was observed in homeostatic and anti-inflammatory microglia as opposed to pro-
423 inflammatory microglia in which all the comets were oriented away from the cell nucleus and
424 toward the cell periphery (23.4%, 12.5% and 0.5%, respectively; $p < 0.001$ Figure S2C). Detection
425 of a pool of retrograde comets in homeostatic microglia suggested the presence of non-centrosomal
426 MT arrays, which we investigated by analyzing the expression and subcellular distribution of
427 endogenous CAMSAP2. Western blot analysis of whole cell lysates revealed endogenous
428 expression of CAMSAP2 in all three microglia phenotypes, with higher protein content in
429 homeostatic microglia (Figure S2D and S7). However, while in homeostatic and anti-inflammatory
430 cells CAMSAP2 often distributed to isolated and clustered puncta along cell ramifications (Figure
431 2C, and 2D arrows), cytosolic CAMSAP2 signal was detectable only around the perinuclear region
432 in pro-inflammatory microglia (Figure 2C and 2D). Radial profiling of CAMSAP2 fluorescence
433 intensity (Figure 2E), used as a measure of CAMSAP2 distribution in the cytosol, confirmed that
434 CAMSAP2 signal decayed more rapidly at increasing distances from the perinuclear region in pro-
435 inflammatory microglia than in homeostatic and anti-inflammatory cells (Figure 2E, and insert).
436 Altogether, these data indicate that homeostatic and anti-inflammatory microglia display a
437 mixed MT polarity pattern resembling neuronal MTs in dendrites and that the acquisition of a pro-
438 inflammatory phenotype represents a unique example of remodeling of the MT cytoskeleton from

439 an array of parallel non-centrosomal MTs to a radial array of MTs all anchored to pericentrosomal
440 MTOCs through their minus ends.
441
442 **Homeostatic microglia nucleate non-centrosomal MTs from Golgi outposts**
443 CAMSAP2 is necessary for the tethering of newly nucleated non-centrosomal MT minus
444 ends during the establishment of polarity in many cell types [51–53]. We investigated the distribution
445 of γ-tubulin, the major MT nucleator in eukaryotic cells, in homeostatic and reactive microglia by
446 confocal microscopy and found that while in homeostatic and anti-inflammatory cells γ-tubulin
447 displayed a punctate distribution around the perinuclear region and along cellular processes, in
448 pro-inflammatory microglia γ-tubulin signal was restricted to the centrosomal and pericentrosomal
449 area (Figure 3A, Figure S3A and Figure 4 and S4). Radial profiling (Figure 3B) of γ-tubulin
450 fluorescence intensity, used as a measure of γ-tubulin signal distribution in the cell, confirmed that
451 γ-tubulin signal decayed more rapidly at increasing distances from the perinuclear region in pro-
452 inflammatory microglia compared to homeostatic and anti-inflammatory cells (Figure 3B, and
453 insert). This observation was confirmed by the analysis of γ-tubulin signal over the cell area
454 (Figure S3B) and detection of higher γ-tubulin levels in homeostatic and anti-inflammatory
455 microglia compared to pro-inflammatory cells (Figure S3C and S7).
456 Altogether, these data demonstrate that the acquisition of a pro-inflammatory phenotype is
457 characterized by restricted localization of γ-tubulin to a pericentrosomal area, which is necessary
458 to establish radial MT arrays. The presence of γ-tubulin in cell ramifications of homeostatic
459 microglia further suggests that microglia are alternatively enriched in non-centrosomal MT
460 nucleation sites, which are necessary to establish non-centrosomal MT arrays.
461 Golgi outposts can serve as acentrosomal MTOCs in other highly polarized brain cells,
462 such as neurons and oligodendrocytes [54–56]. We thus analyzed the distribution of the Golgi marker
463 GM130, a scaffolding protein peripherally associated with Golgi membranes and a marker of
464 Golgi outposts [57]. Co-staining of GM130 with tyrosinated tubulin (Tyr tub) demonstrated that the
465 presence of Golgi outposts is a feature of homeostatic microglia, and that their presence was
466 dramatically reduced in pro-inflammatory cells (Figure 3C and 3D). Importantly, most of the
467 isolated GM130 positive mini-stacks (73.6%) were decorated by γ-tubulin (Figure 3E). To
468 determine whether Golgi outposts could function as MTOCs in homeostatic microglia, MT
469 nucleation was evaluated *in situ* by analyzing MT re-nucleation after nocodazole washout (Figure
470 S3D). We found that both at 15 and 120 mins after nocodazole washout to allow MT-regrowth

471 after nocodazole-induced MT depolymerization, MTs (stained with Tyr tub) emerged from Golgi
472 membranes (GM130 positive) both at pericentrosomal sites and at Golgi outposts located far from
473 the centrosome (Figure 3F). Importantly, γ-tubulin was localized to nucleation-competent Golgi
474 outposts, indicating that non-centrosomal MT re-nucleation did not occur spontaneously at these
475 sites but was strictly dependent on the presence of a γ-tubulin nucleation complex (Figure 3E).

476 These data demonstrate that in homeostatic microglia Golgi outposts can function as sites
477 of acentrosomal MT nucleation and suggest that γ-tubulin-dependent non-centrosomal nucleation
478 is necessary to establish an asymmetric MT array in these cells.

479 To assess whether these *in vitro* observations were representative of MT nucleation in
480 microglia residing in tissue, we analyzed the subcellular distribution of GM130 in retinal
481 microglia: retina and brain share a common embryological origin and similar cell types [58–63].
482 Moreover, retinal neurons are arranged in distinct layers, and microglia are usually restricted to
483 the retinal ganglion cell layer, thus offering an accessible structure for the imaging of their MT
484 cytoskeleton. To identify the microglial cytoskeleton in retina we used cx3cr1$^{gfp/+}$ mice, which
485 constitutively express GFP in microglia. As expected, retinal microglia from control cx3cr1$^{gfp/+}$
486 mice displayed a highly ramified morphology (Figure S3E), typical of homeostatic surveillant cells
487 [6,64,65]. More importantly, confocal immunofluorescence analysis of GM130 signal in retinal GFP
488 positive microglia confirmed the presence of isolated Golgi outposts also in the processes of
489 homeostatic microglia residing in tissue (5 ± 1 per cell, n = 11; Figure 3G, S3F and S3G).

490 Altogether, these results support the notion that MT organization in homeostatic microglia
491 resembles the MT architecture typical of highly polarized, terminally differentiated cells and
492 strongly suggest that γ-tubulin dependent non-centrosomal MT nucleation at Golgi outposts is a
493 *bona fide* feature of homeostatic, surveilling microglia *in vitro* and *in vivo*.

494

495 **Pericentrosomal redistribution of microtubule-nucleating material is a hallmark of pro-**
496 **inflammatory microglia and regulates IL-1β secretion**

497 The recruitment of pericentriolar material (PCM) to the centrosome has been described as
498 a functional step for macrophage activation upon pro-inflammatory stimuli [66]. We thus
499 investigated whether the recruitment of γ-tubulin to a pericentrosomal area was also a hallmark of
500 pro-inflammatory microglia.

501 As revealed by super-resolution microscopy, pro-inflammatory microglia exhibited
502 multiple γ-tubulin^{+} puncta that localized to a perinuclear region (Figure 4A). Quantification of the

503 number of γ-tubulin$^+$ puncta indicated that most pro-inflammatory cells had more than 3 puncta
504 (70 ± 10%; Figure 4B). Conversely, almost all homeostatic and anti-inflammatory microglia
505 displayed only 1 or 2 γ-tubulin$^+$ puncta (95 ± 3% and 96 ± 2%, respectively; Figure 4B). γ-tubulin
506 localization to pericentrosomal puncta showed a time-dependent increase of both number and
507 fluorescence integrated density upon LPS-INFγ challenge (Figure 4C and 4D) and the recruitment
508 of γ-tubulin$^+$ puncta was dependent on a dynamic MT cytoskeleton because a low dose of taxol
509 was sufficient to inhibit it (Figure S4A and S4B). Notably, in most pro-inflammatory cells with
510 >2 γ-tubulin$^+$ puncta (65 ± 10%; Figure S4C) the centrosomal marker centrin-3 localized only to
511 ≤2 γ-tubulin$^+$ puncta. In addition, while a quarter of pro-inflammatory cells was proliferating (23
512 ± 4%; Figure S4E and S4F), most pro-inflammatory microglia displayed >2 γ-tubulin$^+$ puncta (70
513 ± 10%; Figure 4B) and ≤2 centrin$^+$ puncta (Figure S4D). Conversely, PCM localization to γ-
514 tubulin$^+$ puncta was confirmed by coimmunostaining with pericentrin (86 ± 5% of colocalizing
515 puncta), a conserved PCM scaffold protein necessary for MTOC assembly and maturation [67]
516 Figure S4G). Indeed, both centrin$^+$ and centrin$^-$ γ-tubulin$^+$ puncta localized to the center of MT
517 asters (Fig. S4H) and MT re-growth after nocodazole washout (Figure S4I,J) revealed that *de novo*
518 MT nucleation occurred at γ-tubulin$^+$ puncta (Figure S4L). This indicated that γ-tubulin
519 reorganization in pro-inflammatory microglia is ascribed to PCM maturation that is uncoupled
520 from cell or centrosome duplication, and that *de novo* generated PCM puncta act as MTOCs.

521 Perinuclear γ-tubulin redistribution was also observed in proinflammatory microglia in a
522 mouse model of retinal inflammation. For this, we took advantage of a well-established protocol
523 of acute inflammatory uveitis [32–37] induced by intravitreal injection of LPS (Figure S5A) to activate
524 retinal microglia towards the pro-inflammatory phenotype. Microglia residing in retinal slices
525 from LPS-treated mice acquired an amoeboid morphology with reduced branching complexity, as
526 revealed by skeleton analysis of Iba1 positive cells (Figure S5B and S5C). Moreover, co-
527 immunolabelling with Iba1 and γ-tubulin demonstrated that while in control (sham) mice retinal
528 microglia displayed punctate diffuse γ-tubulin staining along cellular ramifications (Figure 4E), in
529 LPS treated mice microglia clearly exhibited a condensed γ-tubulin pattern, clustered around a
530 perinuclear region (Figure 4E). This was confirmed by quantitative analysis of γ-tubulin signal
531 over the cell area and of the number of γ-tubulin$^+$ puncta per cell (Figure 4F).

532 In summary, these data demonstrate that the presence of pericentrosomal MTOC maturation
533 is a *bona fide* feature of pro-inflammatory microglia *in vitro* and *in vivo*.

534 Next, we examined if maturation of pericentrosomal MTOCs was a regulatory step for
535 microglia acquisition of the pro-inflammatory phenotype. To this end, we treated microglia with
536 the selective PLK4 inhibitor centrinone to hamper PCM maturation [68] prior to LPS-INFγ
537 stimulation (Figure 5A) and measured its effects on EV blebbing and cytokine release (Figure 5).
538 First, we found that centrinone increased the number (4.7-fold; Figure 5C, top) and reduced the
539 diameter (by 30%; Figure 5C, bottom) of EVs blebbing from the cell surface of pro-inflammatory
540 microglia (Fig. 5A-C). Activation of NLRP3-inflammasome is a characteristic feature of pro-
541 inflammatory microglia and macrophages [69–73] and the centrosome-associated protein kinase
542 NEK7 is required for NLRP3–inflammasome activation (for review see [62]). In addition, NLRP3
543 activation is required for IL-1β maturation in immortalized and primary microglia [69,75], and
544 inhibition of PLK4 leads to NLRP3 hyper-activation through NEK7 dephosphorylation in bone
545 marrow-derived macrophages [68]. We then measured NLRP3-inflammasome protein levels in
546 homeostatic and pro-inflammatory microglia upon centrinone treatment. We found that in
547 homeostatic microglia, LPS-IFNγ but not centrinone alone increased NLRP3 expression while
548 centrinone / LPS-IFNγ co-treatment enhanced NLRP3 more than LPS-IFNγ alone (Figure 5D and
549 S7), suggesting that inhibition of PCM maturation induces NLRP3 hyperactivation in pro-
550 inflammatory microglia. We investigated whether PLK4 inhibition modulates microglia IL-
551 1β release and found that co-treatment with centrinone enhanced pro-inflammatory microglia-
552 mediated IL-1β release, without affecting IL-1β release from homeostatic cells (Figure 5E). In
553 addition, we observed that centrinone did not modulate the release of IL-10 and IL-6 (Figure 5F),
554 indicating that PLK4 inhibition enhances pro-inflammatory microglia IL-1β release through
555 NLRP3-inflammasome activation but has no effect on NLRP3-independent pathways.
556 Together, these data demonstrate that microglia pro-inflammatory reactivity induces PCM
557 maturation *in vivo* and *in vitro*, and that this step is a negative regulator of NLRP3-dependent IL-
558 1β release. They also indicate that remodeling of the MT cytoskeleton during pro-inflammatory
559 reactivity is temporally coupled to cytokine release, providing a novel potential target of microglia
560 treatment in inflammatory diseases.
561
562 **DISCUSSION**
563 Here we describe the reorganization of the microglial MT cytoskeleton that characterizes
564 the transitions between homeostatic, pro-inflammatory and anti-inflammatory states, and
565 demonstrate the functional interplay between microglial PCM maturation and pro-inflammatory

566 reactivity. Our findings demonstrate that pro-inflammatory microglia reactivity orchestrates a so
567 far unique rearrangement of the MT cytoskeleton from a non-centrosomal array of parallel and
568 stable MTs nucleated at Golgi outposts characteristic of the homeostatic state, to a radial array in
569 which MTs are anchored to *de novo* formed pericentrosomal MTOCs through their minus ends.
570 Through *in vitro* phenotyping and *in vivo* validation, we report four main findings summarized in
571 Figure S6: 1) Homeostatic microglia possess stable MT arrays, while microglia reactivity increases
572 MT dynamic behavior. 2) Non-centrosomal MT organization in arrays with mixed polarity is a
573 feature of homeostatic microglia, like the architecture typical of highly specialized cells such as
574 neurons and oligodendrocytes. 3) Pro-inflammatory microglia reactivity results in restricted γ-
575 tubulin localization to puncta around the centrosome because of *de novo* PCM and MTOC
576 maturation, providing a novel distinct marker of microglia reactivity in live-imaging studies 4)
577 PCM maturation in pro-inflammatory microglia is a regulator of NLRP3-dependent IL-1β release.

578 To date, only circumscribed evidence has suggested that ramified microglia possess more
579 acetylated and detyrosinated MTs than ameboid pro-inflammatory cells [14,76]. Here, we show that
580 homeostatic ramified microglia display higher levels of tubulin acetylation and detyrosination, two
581 indirect indicators of "older", i.e., more stable and less dynamic, MT subpopulations [49,77].
582 Moreover, we report that during classical and alternative activation obtained with either LPS-IFNγ
583 or IL-4 stimulation respectively [78–80], microglia MTs become less stable and more dynamic,
584 suggesting that the acquisition of new cellular functions induces changes in MT stability *via*
585 modulation of MT dynamics [81].

586 We describe that homeostatic/ramified microglial MTs exhibit an asymmetric dendrite-like
587 organization characterized by EB1 comets arranged in mixed polarity with the minus-end capping
588 protein CAMPSAP2 localized at branching points and cell ramifications. In anti-inflammatory
589 microglia, we find lower levels of CAMSAP2 that localize in a similar fashion in bipolar processes.
590 The presence of CAMSAP2 in microglia processes might suggest that, as in neurons [51,82–86],
591 stabilization of non-centrosomal MTs at their minus ends is important to achieve elongated bipolar
592 morphology, typical of anti-inflammatory microglia, and for the formation of long branched
593 cellular extensions patrolling brain parenchyma in homeostatic microglia.

594 We find that the acquisition of a pro-inflammatory phenotype disrupts the cellular
595 asymmetry of homeostatic microglia and reduces the pool of non-centrosomal, parallel and mixed
596 oriented MTs, leading to their rearrangement into a radial array of uniformly oriented MTs
597 characteristic of the ameboid shape. In addition, while in pro-inflammatory microglia all the MTs

598 are anchored to a centrosomal region, homeostatic microglia nucleate acentrosomal MTs from
599 Golgi outposts located far from the cell body at the branching points of microglia ramifications,
600 resembling the structure of the dendritic tree of mature neurons [51,87,88] or the organization of
601 oligodendrocytic myelin sheaths [55,56]. This Golgi outpost-dependent non-centrosomal nucleation
602 contrasts to pro-inflammatory and anti-inflammatory microglia in which the Golgi apparatus
603 displays a compact perinuclear location [89], suggesting that in reactive microglia cellular
604 arborization is reduced by restricting the Golgi to a region adjacent to the centrosome, which acts
605 as the major MT nucleator in these cells. Indeed, we observed that the acquisition of a pro-
606 inflammatory phenotype is characterized by γ-tubulin redistribution to puncta located to a
607 pericentrosomal region, a feature we confirmed in retinal microglia residing in tissue. Co-
608 localization of γ-tubulin with pericentrin and *de novo* nucleation of radial MTs from γ-tubulin^{+}
609 puncta upon nocodazole washout strongly suggests that these protein assemblies are composed of
610 PCM and act as pericentrosomal MTOCs. Importantly, γ-tubulin redistribution during the
611 transition to a pro-inflammatory phenotype did not derive from centriolar duplication during cell
612 division [90,91] as no more than 2 γ-tubulin^{+} puncta colocalized with centrin-3 in the same cell, an
613 abundant protein associated with the centrosome [92]. In addition, γ-tubulin redistribution was
614 strictly dependent on a dynamic MT cytoskeleton, suggesting that the increase in MT dynamicity
615 is necessary for the relocation of MT nucleating material to the centrosome. Importantly, our
616 observations indicate that pericentrosomal redistribution of microtubule nucleating material may
617 further provide a distinct and highly valuable live-imaging marker of microglia activation to detect
618 progression of neuroinflammatory disease and efficacy of therapeutics over time.

619 We find that PCM maturation occurring in pro-inflammatory microglia negatively
620 regulates IL-1β release through a non-classical secretory pathway [93]. Indeed, inhibition of PLK4
621 during the acquisition of a pro-inflammatory phenotype reduces pericentrosomal γ-tubulin^{+} puncta
622 formation, increases NLRP3 expression, and potentiates IL-1β release without affecting the
623 release of IL-6 and IL-10. NLRP3-inflammasome hyperactivation is consistent with NLRP3
624 hyperactivation through NEK7 dephosphorylation by inhibition of PLK4 in macrophages [68,74].
625 Given that the NLRP3-inflammasome mediates interleukin activation [94], NLRP3-inflammasome
626 hyperactivation may account for the increase in IL-1β release and the accumulation of blebbing
627 microvesicles we observe in microglia stimulated *in vitro*. Interestingly, our results on cytokine
628 release upon PLK4-inhibition differ from those reported after long-term (7 days) inhibition in
629 macrophages activated with LPS [66] suggesting that the response to loss of PLK4 activity is cell

630 type specific or longer treatments may have either secondary or opposite effects. Further studies
631 are necessary to discriminate between these possibilities.

632 In summary, we identify a heretofore unique example of MT reorganization from a non-
633 centrosomal array of MTs with mixed polarity to a radial array in which all the MTs are uniformly
634 oriented and anchored either at the centrosome or pericentrosomal MTOCs. Our structural,
635 functional and in tissue analyses further demonstrate that acentrosomal MT nucleation at Golgi
636 outposts may play an important role in supporting the patrolling phenotype of microglia cells, that
637 tubulin remodeling enables microglia reactivity *in vitro* and in tissue, and that targeting PCM
638 maturation in reactive microglia may represent a new approach to limit tissue damage during
639 neurodegenerative disease in which microgliosis contributes to neuronal injury and cognitive
640 decline [2,12]. In addition, given the newly identified role for a population of spinal $CD11c^+$ microglia
641 in the remission and recurrence of neuropathic pain [95], it will be become critical to determine the
642 contribution of spinal microglial MT dysfunction in the peripheral neuropathy caused by
643 chemotherapeutic drugs, most of which target the MT cytoskeleton.

644

645 **Acknowledgments:** The authors wish to thank the Animal Facility of Physiology and
646 Pharmacology Department of Sapienza University. The graphical abstract in Figure S6 was created
647 using BioRender.com. We are grateful to David Sulzer for comments on the manuscript and useful
648 discussions. Further information and requests for resources and reagents should be directed to and
649 will be fulfilled by the lead contact, Silvia Di Angelantonio (silvia.diangelantonio@uniroma1.it).

650 This study was supported by NIH/NIA R56AG050658 and NIH/NINDS R21 NS120076-01 grants
651 to FB and a Fulbright Award to FB and SDA. This research was also funded by the CrestOptics-
652 IIT JointLab for Advanced Microscopy (to SDA and GCR); the Regione Lazio MARBEL
653 Life2020 and Bio3DBrain FSE 2014-2020 grants (to SDA); by Sapienza University
654 RM118163E0297F84 and PH12017270934C3C grants (to SDA) and Fondazione Istituto Italiano
655 di Tecnologia (to MR and CS). CS was also supported by the Ph.D. program in Life Science at
656 Sapienza University in Rome. The research leading to these results has been also supported by
657 European Research Council Synergy grant ASTRA (n. 855923 to GCR.).

658 **Author contributions:** FB, SDA, and MR designed the study and wrote the manuscript. CS, MR,
659 MM, DD, FC, GP, MG and AI performed experiments and generated primary data. GG generated
660 code; CS, MR, FC, DD, GP, MM, MG and SDA performed data analysis. EDL, SDP, GCR, DR,

661 and RG provided helpful insights and contributed key techniques. FB and SDA supervised data
662 analysis and experiments.

663 **Competing interests:** Authors declare that they have no competing interests.

664 **Data and materials availability:** This study did not generate new unique reagents. The data that
665 support the findings of this study are available from the corresponding author upon reasonable
666 request. The code is available at https://github.com/ggosti/maxIntensityRadialProfile.

667

668 **References**

669 1 Bolasco G, Weinhard L, Boissonnet T, Neujahr R, Gross CT. Three-dimensional
670 nanostructure of an intact microglia cell. *Front Neuroanat* 2018; **12**: 1–5.
671 2 Colonna M, Butovsky O. Microglia function in the central nervous system during health
672 and neurodegeneration. *Annu Rev Immunol* 2017; **35**: 441–468.
673 3 Nimmerjahn A, Kirchhoff F, Helmchen F. Resting microglial cells are highly dynamic
674 surveillants of brain parenchyma in vivo. *Neuroforum* 2005; **11**: 95–96.
675 4 Paolicelli RC, Bolasco G, Pagani F, Maggi L, Scianni M, Panzanelli P *et al.* Synaptic
676 pruning by microglia is necessary for normal brain development. *Science (80-)* 2011; **333**:
677 1456–1458.
678 5 Parkhurst CN, Yang G, Ninan I, Savas JN, Yates JR, Lafaille JJ *et al.* Microglia promote
679 learning-dependent synapse formation through brain-derived neurotrophic factor. *Cell*
680 2013; **155**: 1596–1609.
681 6 Basilico B, Pagani F, Grimaldi A, Cortese B, Di Angelantonio S, Weinhard L *et al.*
682 Microglia shape presynaptic properties at developing glutamatergic synapses. *Glia* 2019;
683 **67**: 53–67.
684 7 Bernier LP, Bohlen CJ, York EM, Choi HB, Kamyabi A, Dissing-Olesen L *et al.*
685 Nanoscale Surveillance of the Brain by Microglia via cAMP-Regulated Filopodia. *Cell*
686 *Rep* 2019; **27**: 2895-2908.e4.
687 8 Basilico B, Ferrucci L, Ratano P, Golia MT, Grimaldi A, Rosito M *et al.* Microglia
688 control glutamatergic synapses in the adult mouse hippocampus. *Glia* 2021; : 1–23.
689 9 Davalos D, Grutzendler J, Yang G, Kim J V., Zuo Y, Jung S *et al.* ATP mediates rapid
690 microglial response to local brain injury in vivo. *Nat Neurosci* 2005; **8**: 752–758.
691 10 Madry C, Kyrargyri V, Arancibia-Cárcamo IL, Jolivet R, Kohsaka S, Bryan RM *et al.*

692 Microglial Ramification, Surveillance, and Interleukin-1β Release Are Regulated by the
693 Two-Pore Domain K+ Channel THIK-1. *Neuron* 2018; **97**: 299-312.e6.
694 11 Kettenmann H, Hanisch U-K, Noda M, Verkhratsky A. Physiology of Microglia. *Physiol*
695 *Rev* 2011; **91**: 461–553.
696 12 Heneka MT, Kummer MP, Latz E. Innate immune activation in neurodegenerative
697 disease. *Nat Rev Immunol* 2014; **14**: 463–477.
698 13 Li R, Gundersen GG. Beyond polymer polarity: How the cytoskeleton builds a polarized
699 cell. *Nat Rev Mol Cell Biol* 2008; **9**: 860–873.
700 14 Ilschner S, Brandt R. The transition of microglia to a ramified phenotype is associated
701 with the formation of stable acetylated and detyrosinated microtubules. *Glia* 1996; **18**:
702 129–140.
703 15 Nogales E, Whittaker M, Milligan RA, Downing KH. High-resolution model of the
704 microtubule. *Cell* 1999; **96**: 79–88.
705 16 Klinman E, Holzbaur ELF. Walking Forward with Kinesin. *Trends Neurosci* 2018; **41**:
706 555–556.
707 17 Reck-Peterson SL, Redwine WB, Vale RD, Carter AP. The cytoplasmic dynein transport
708 machinery and its many cargoes. *Nat Rev Mol Cell Biol* 2018; **19**: 382–398.
709 18 Mitchison T, Kirschner M. Dynamic instability of microtubule growth. *Nature* 1984; **312**:
710 237–242.
711 19 Janke C, Magiera MM. The tubulin code and its role in controlling microtubule properties
712 and functions. *Nat Rev Mol Cell Biol* 2020; **21**: 307–326.
713 20 Gadadhar S, Bodakuntla S, Natarajan K, Janke C. The tubulin code at a glance. *J Cell Sci*
714 2017; **130**: 1347 LP – 1353.
715 21 Janke C, Bulinski JC. Post-translational regulation of the microtubule cytoskeleton:
716 Mechanisms and functions. *Nat Rev Mol Cell Biol* 2011; **12**: 773–786.
717 22 Etienne-Manneville S. Microtubules in cell migration. *Annu Rev Cell Dev Biol* 2013; **29**:
718 471–499.
719 23 Meiring JCM, Akhmanova A. Microtubules keep large cells in shape. *J Cell Biol* 2020;
720 **219**: 1–3.
721 24 Akhmanova A, Hoogenraad CC. Microtubule minus-end-targeting proteins. *Curr Biol*
722 2015; **25**: R162–R171.
723 25 Alieva IB, Berezinskaya T, Borisy GG, Vorobjev IA. Centrosome nucleates numerous

724 ephemeral microtubules and only few of them participate in the radial array. *Cell Biol Int*
725 2015; **39**: 1203–1216.
726 26 Vinogradova T, Miller PM, Kaverina I. Microtubule network asymmetry in motile cells:
727 Role of Golgi-derived array. *Cell Cycle* 2009; **8**: 2168–2174.
728 27 Bartolini F, Gundersen GG. Generation of noncentrosomal microtubule arrays. *J Cell Sci*
729 2006; **119**: 4155–4163.
730 28 Akhmanova A, Steinmetz MO. Microtubule minus-end regulation at a glance. *J Cell Sci*
731 2019; **132**: 1–7.
732 29 Rosito M, Deflorio C, Limatola C, Trettel F. CXCL16 orchestrates adenosine A 3 receptor
733 and MCP-1/CCL2 activity to protect neurons from excitotoxic cell death in the CNS. *J*
734 *Neurosci* 2012; **32**: 3154–3163.
735 30 Zhu X, Kaverina I. Quantification of asymmetric microtubule nucleation at subcellular
736 structures. *Methods Mol Biol* 2011; **777**: 235–244.
737 31 Pagani F, Paolicelli RC, Murana E, Cortese B, Di Angelantonio S, Zurolo E *et al.*
738 Defective microglial development in the hippocampus of Cx3cr1 deficient mice. *Front*
739 *Cell Neurosci* 2015; **9**: 1–14.
740 32 Becker MD, Garman K, Whitcup SM, Planck SR, Rosenbaum JT. Inhibition of leukocyte
741 sticking and infiltration, but not rolling, by antibodies to ICAM-1 and LFA-1 in murine
742 endotoxin-induced uveitis. *Investig Ophthalmol Vis Sci* 2001; **42**: 2563–2566.
743 33 Rosenbaum JT, Woods A, Kezic J, Planck SR, Rosenzweig HL. Contrasting Ocular
744 Effects of Local versus Systemic Endotoxin. *Investig Ophthalmol Vis Sci* 2011; **52**: 6472–
745 6477.
746 34 Wang M, Ma W, Zhao L, Fariss RN, Wong WT. Adaptive Müller cell responses to
747 microglial activation mediate neuroprotection and coordinate inflammation in the retina. *J*
748 *Neuroinflammation* 2011; **8**: 173.
749 35 Chu CJ, Gardner PJ, Copland DA, Liyanage SE, Gonzalez-Cordero A, Holthaus SMK *et*
750 *al.* Multimodal analysis of ocular inflammation using the endotoxin-induced uveitis
751 mouse model. *DMM Dis Model Mech* 2016; **9**: 473–481.
752 36 Bell OH, Copland DA, Ward A, Nicholson LB, Lange CAK, Chu CJ *et al.* Single Eye
753 mRNA-Seq Reveals Normalisation of the Retinal Microglial Transcriptome Following
754 Acute Inflammation. *Front Immunol* 2020; **10**. doi:10.3389/fimmu.2019.03033.
755 37 Wu Y, Zheng X, Ding Y, Zhou M, Wei Z, Liu T *et al.* The molecular chaperone Hsp90α

756 deficiency causes retinal degeneration by disrupting Golgi organization and vesicle
757 transportation in photoreceptors. *J Mol Cell Biol* 2020; **12**: 216–229.
758 38 Ingaramo M, York AG, Hoogendoorn E, Postma M, Shroff H, Patterson GH. Richardson-
759 Lucy deconvolution as a general tool for combining images with complementary
760 strengths. *ChemPhysChem* 2014; **15**: 794–800.
761 39 Ströhl F, Kaminski CF. A joint Richardson-Lucy deconvolution algorithm for the
762 reconstruction of multifocal structured illumination microscopy data. *Methods Appl*
763 *Fluoresc* 2015; **3**: 14002.
764 40 Chakrova N, Rieger B, Stallinga S. Deconvolution methods for structured illumination
765 microscopy. *J Opt Soc Am A* 2016; **33**: B12.
766 41 Heintzmann R, Benedetti PA. High-resolution image reconstruction in fluorescence
767 microscopy with patterned excitation. *Appl Opt* 2006; **45**: 5037–5045.
768 42 Schindelin J, Arganda-Carreras I, Frise E, Kaynig V, Longair M, Pietzsch T *et al.* Fiji: An
769 open-source platform for biological-image analysis. *Nat Methods* 2012; **9**: 676–682.
770 43 Otsu N. A Threshold Selection Method from Gray-Level Histograms. *IEEE Trans Syst*
771 *Man Cybern* 1979; **9**: 62–66.
772 44 Dhamodharan R, Wadsworth P. Modulation of microtubule dynamic instability in vivo by
773 brain microtubule associated proteins. *J Cell Sci* 1995; **108**: 1679–1689.
774 45 Rusan NM, Fagerstrom CJ, Yvon AMC, Wadsworth P. Cell cycle-dependent changes in
775 microtubule dynamics in living cells expressing green fluorescent protein-α tubulin. *Mol*
776 *Biol Cell* 2001; **12**: 971–980.
777 46 Schmittgen TD, Livak KJ. Analyzing real-time PCR data by the comparative CT method.
778 *Nat Protoc* 2008; **3**: 1101–1108.
779 47 Bohlen CJ, Bennett FC, Tucker AF, Collins HY, Mulinyawe SB, Barres BA. Diverse
780 Requirements for Microglial Survival, Specification, and Function Revealed by Defined-
781 Medium Cultures. *Neuron* 2017; **94**: 759-773.e8.
782 48 Herr DR, Yam TYA, Tan WSD, Koh SS, Wong WSF, Ong WY *et al.* Ultrastructural
783 Characteristics of DHA-Induced Pyroptosis. *NeuroMolecular Med* 2020; **22**: 293–303.
784 49 Webster DR, Borisy GG. Microtubules are acetylated in domains that turn over slowly. *J*
785 *Cell Sci* 1989; **92 (Pt 1)**: 57–65.
786 50 Lukinavičius G, Reymond L, D'Este E, Masharina A, Göttfert F, Ta H *et al.* Fluorogenic
787 probes for live-cell imaging of the cytoskeleton. *Nat Methods* 2014; **11**: 731–733.

788 51 Yau KW, vanBeuningen SFB, Cunha-Ferreira I, Cloin BMC, vanBattum EY, Will L *et al.*
789 Microtubule minus-end binding protein CAMSAP2 controls axon specification and
790 dendrite development. *Neuron* 2014; **82**: 1058–1073.
791 52 Tanaka N, Meng W, Nagae S, Takeichi M. Nezha/CAMSAP3 and CAMSAP2 cooperate
792 in epithelial-specific organization of noncentrosomal microtubules. *Proc Natl Acad Sci U*
793 *S A* 2012; **109**: 20029–20034.
794 53 Martin M, Veloso A, Wu J, Katrukha EA, Akhmanova A. Control of endothelial cell
795 polarity and sprouting angiogenesis by noncentrosomal microtubules. *Elife* 2018; **7**: 1–37.
796 54 Ori-McKenney KM, Jan LY, Jan YN. Golgi Outposts Shape Dendrite Morphology by
797 Functioning as Sites of Acentrosomal Microtubule Nucleation in Neurons. *Neuron* 2012;
798 **76**: 921–930.
799 55 Fu M meng, McAlear TS, Nguyen H, Oses-Prieto JA, Valenzuela A, Shi RD *et al.* The
800 Golgi Outpost Protein TPPP Nucleates Microtubules and Is Critical for Myelination. *Cell*
801 2019; **179**: 132-146.e14.
802 56 Valenzuela A, Meservey L, Nguyen H, Fu M meng. Golgi Outposts Nucleate
803 Microtubules in Cells with Specialized Shapes. *Trends Cell Biol* 2020; **30**: 792–804.
804 57 Wu J, Akhmanova A. Microtubule-Organizing Centers. *Annu Rev Cell Dev Biol* 2017; **33**:
805 51–75.
806 58 Sernagor E, Eglen SJ, Wong ROL. Development of retinal ganglion cell structure and
807 function. *Prog Retin Eye Res* 2001; **20**: 139–174.
808 59 Kavcic V, Vaughn W, Duffy CJ. Distinct visual motion processing impairments in aging
809 and Alzheimer's disease. *Vision Res* 2011; **51**: 386–395.
810 60 Lee DH, Laemmer AB, Waschbisch A, Struffert T, Maihöfner C, Schwab S *et al.*
811 Neuromyelitis optica presenting with relapses under treatment with natalizumab: A case
812 report. *J Med Case Rep* 2014; **8**: 2–4.
813 61 Javaid FZ, Brenton J, Guo L, Cordeiro MF. Visual and ocular manifestations of
814 Alzheimer's disease and their use as biomarkers for diagnosis and progression. *Front*
815 *Neurol* 2016; **7**. doi:10.3389/fneur.2016.00055.
816 62 Chang LYL, Lowe J, Ardiles A, Lim J, Grey AC, Robertson K *et al.* Alzheimer's disease
817 in the human eye. Clinical tests that identify ocular and visual information processing
818 deficit as biomarkers. *Alzheimer's Dement* 2014; **10**: 251–261.
819 63 Bambo MP, Garcia-Martin E, Otin S, Pinilla J, Larrosa JM, Polo V *et al.* Visual function

820 and retinal nerve fibre layer degeneration in patients with Alzheimer disease: correlations
821 with severity of dementia. *Acta Ophthalmol* 2015; **93**: e507–e508.
822 64 Cordella F, Sanchini C, Rosito M, Ferrucci L, Pediconi N, Cortese B *et al.* Antibiotics
823 Treatment Modulates Microglia–Synapses Interaction. *Cells* 2021; **10**: 2648.
824 65 Grimaldi A, Brighi C, Peruzzi G, Ragozzino D, Bonanni V, Limatola C *et al.*
825 Inflammation, neurodegeneration and protein aggregation in the retina as ocular
826 biomarkers for Alzheimer's disease in the 3xTg-AD mouse model. *Cell Death Dis* 2018;
827 **9**. doi:10.1038/s41419-018-0740-5.
828 66 Vertii A, Ivshina M, Zimmerman W, Hehnly H, Kant S, Doxsey S. The Centrosome
829 Undergoes Plk1-Independent Interphase Maturation during Inflammation and Mediates
830 Cytokine Release. *Dev Cell* 2016; **37**: 377–386.
831 67 Zimmerman WC, Sillibourne J, Rosa J, Doxsey SJ. Mitosis-specific Anchoring of γ
832 Tubulin Complexes by Pericentrin Controls Spindle Organization and Mitotic Entry. *Mol*
833 *Biol Cell* 2004; **15**: 3642–3657.
834 68 Yang X, Li W, Zhang S, Wu D, Jiang X, Tan R *et al.* PLK 4 deubiquitination by Spata2-
835 CYLD suppresses NEK7-mediated NLRP3 inflammasome activation at the centrosome .
836 *EMBO J* 2020; **39**: 1–16.
837 69 Gustin A, Kirchmeyer M, Koncina E, Felten P, Losciuto S, Heurtaux T *et al.* NLRP3
838 inflammasome is expressed and functional in mouse brain microglia but not in astrocytes.
839 *PLoS One* 2015; **10**: 1–19.
840 70 Hanslik KL, Ulland TK. The Role of Microglia and the Nlrp3 Inflammasome in
841 Alzheimer's Disease. *Front Neurol* 2020; **11**: 1–9.
842 71 Schroder K, Tschopp J. The Inflammasomes. *Cell* 2010; **140**: 821–832.
843 72 Davis BK, Wen H, Ting JP-Y. The Inflammasome NLRs in Immunity, Inflammation, and
844 Associated Diseases. *Annu Rev Immunol* 2011; **29**: 707–735.
845 73 Latz E, Xiao TS, Stutz A. Activation and regulation of the inflammasomes. *Nat Rev*
846 *Immunol* 2013; **13**: 397–411.
847 74 Seoane PI, Lee B, Hoyle C, Yu S, Lopez-Castejon G, Lowe M *et al.* The NLRP3-
848 inflammasome as a sensor of organelle dysfunction. *J Cell Biol* 2020; **219**: 1–12.
849 75 Ji X, Song Z, He J, Guo S, Chen Y, Wang H *et al.* NIMA-related kinase 7 amplifies
850 NLRP3 inflammasome pro-inflammatory signaling in microglia/macrophages and mice
851 models of spinal cord injury. *Exp Cell Res* 2021; **398**: 14–22.

852 76 Yu Z, Yang L, Yang Y, Chen S, Sun D, Xu H *et al.* Epothilone B Benefits Nigral
853 Dopaminergic Neurons by Attenuating Microglia Activation in the 6-Hydroxydopamine
854 Lesion Mouse Model of Parkinson's Disease. *Front Cell Neurosci* 2018; **12**: 1–13.
855 77 Baas PW, Rao AN, Matamoros AJ, Leo L. Stability properties of neuronal microtubules.
856 *Cytoskeleton* 2016; **73**: 442–460.
857 78 Durafourt BA, Moore CS, Zammit DA, Johnson TA, Zaguia F, Guiot MC *et al.*
858 Comparison of polarization properties of human adult microglia and blood-derived
859 macrophages. *Glia* 2012; **60**: 717–727.
860 79 Gordon S, Taylor PR. Monocyte and macrophage heterogeneity. *Nat Rev Immunol* 2005;
861 **5**: 953–964.
862 80 Perry VH, Nicoll JAR, Holmes C. Microglia in neurodegenerative disease. *Nat Rev*
863 *Neurol* 2010; **6**: 193–201.
864 81 Li L, Yang XJ. Tubulin acetylation: Responsible enzymes, biological functions and
865 human diseases. *Cell Mol Life Sci* 2015; **72**: 4237–4255.
866 82 Jiang K, Hua S, Mohan R, Grigoriev I, Yau KW, Liu Q *et al.* Microtubule Minus-End
867 Stabilization by Polymerization-Driven CAMSAP Deposition. *Dev Cell* 2014; **28**: 295–
868 309.
869 83 Baas PW, Deitch JS, Black MM, Banker GA. Polarity orientation of microtubules in
870 hippocampal neurons: Uniformity in the axon and nonuniformity in the dendrite. *Proc*
871 *Natl Acad Sci U S A* 1988; **85**: 8335–8339.
872 84 Baas PW, Slaughter T, Brown A, Black MM. Microtubule dynamics in axons and
873 dendrites. *J Neurosci Res* 1991; **30**: 134–153.
874 85 Burton PR, Paige JL. Polarity of axoplasmic microtubules in the olfactory nerve of the
875 frog. *Proc Natl Acad Sci* 1981; **78**: 3269–3273.
876 86 Heidemann SR, Landers JM, Hamborg MA. Polarity orientation of axonal microtubules. *J*
877 *Cell Biol* 1981; **91**: 661–665.
878 87 Horton AC, Rácz B, Monson EE, Lin AL, Weinberg RJ, Ehlers MD. Polarized secretory
879 trafficking directs cargo for asymmetric dendrite growth and morphogenesis. *Neuron*
880 2005; **48**: 757–771.
881 88 Nguyen MM, McCracken CJ, Milner ES, Goetschius DJ, Weiner AT, Long MK *et al.* γ-
882 tubulin controls neuronal microtubule polarity independently of Golgi outposts. *Mol Biol*
883 *Cell* 2014; **25**: 2039–2050.

884 89 Li J, Ahat E, Wang Y. *Golgi structure and function in health, stress, and diseases*. 2019
885 doi:10.1007/978-3-030-23173-6_19.
886 90 Fuller SD, Gowen BE, Reinsch S, Sawyer A, Buendia B, Wepf R *et al.* The core of the
887 mammalian centriole contains γ-tubulin. *Curr Biol* 1995; **5**: 1384–1393.
888 91 Alvarado-Kristensson M. Γ-Tubulin As a Signal-Transducing Molecule and Meshwork
889 With Therapeutic Potential. *Signal Transduct Target Ther* 2018; **3**: 1–6.
890 92 Middendorp S, Küntziger T, Abraham Y, Holmes S, Bordes N, Paintrand M *et al.* A role
891 for centrin 3 in centrosome reproduction. *J Cell Biol* 2000; **148**: 405–415.
892 93 Lacy P, Stow JL. Cytokine release from innate immune cells: Association with diverse
893 membrane trafficking pathways. *Blood* 2011; **118**: 9–18.
894 94 Hanisch UK. Microglia as a source and target of cytokines. *Glia* 2002; **40**: 140–155.
895 95 Kohno K, Shirasaka R, Yoshihara K, Mikuriya S, Tanaka K, Takanami K *et al.* A spinal
896 microglia population involved in remitting and relapsing neuropathic pain. *Science* 2022;
897 **376**: 86–90.
898
899 **Figure 1. Homeostatic, pro-inflammatory and anti-inflammatory primary microglia differ
900 in MT distribution, stability and dynamic behavior.**
901 **(A)** Representative images of tyrosinated α-tubulin (Tyr tub, green) staining in homeostatic
902 (Homeo), pro-inflammatory (Pro-inf) and anti-inflammatory (Anti-inf) microglia (*top*; scale bar:
903 20 µm) and corresponding masks (MASKS) used for the analysis (*bottom*), with radial scale (unit
904 = 5 µm; blue circles) centered at the centroid of the cell nucleus. Red circle indicates the radius
905 corresponding to the largest intensity value. **(B)** Plot showing maximum fluorescence intensity
906 values of Tyr tub vs the radial distance from cell nucleus, obtained with radial profiling, in Homeo
907 (n = 38, green), Pro-inf (n = 31, magenta) and Anti-inf (n = 38, blue) microglia. Curve fit was
908 performed using a single exponential decay function. *Insert:* bar chart reporting the exponential
909 decay constant values (K) for each condition (values are expressed as mean ± SEM from 4
910 independent experiments; *** p <0.001, One-way ANOVA – Tukey's multiple comparison test).
911 Note faster decay of Tyr tub signal in Pro-inf microglia. **(C)** Representative immunofluorescence
912 images of Homeo, Pro-inf e Anti-inf microglia: *left*, co-staining of Tyr tub (green) and de-
913 tyrosinated tubulin (Detyr, magenta) (scale bar: 20 µm. Hoechst for nuclei visualization, blue);
914 *right*, co-staining of Tyr tub (green) and acetylated tubulin (Acetyl, magenta) (scale bar: 20 µm.
915 Hoechst for nuclei visualization, blue). Cell outlines are indicated by white dashed line. **(D)** Scatter

916 dot plots showing immunofluorescence signal quantification of detyrosinated/ tyrosinated
917 (Detyr/Tyr) tub ratio (*left*, Homeo n = 19, Pro-inf n = 32, Anti-inf n = 28 cells from 3 independent
918 experiments) and acetylated/tyrosinated (Acetyl/Tyr) tubulin ratio (*right*; Homeo n = 33, Pro-inf
919 n = 25, Anti-inf n = 29 cells from 3 independent experiments). Values are expressed as median ±
920 interquartile range; *** p <0.001; Kruskall-Wallis - Dunn's multiple comparisons test. Note that
921 Pro- and Anti-inf microglia have reduced tubulin PTM levels with respect to Homeo cells. **(E)**
922 Representative inverted contrast widefield frames from time lapse acquisitions of SiRtubulin in
923 Homeo, Pro-inf and Anti-inf microglia at 4 different timepoints (0 s, 20 s, 40 s, 60 s). Red lines
924 highlight MT length changes ≥0.5 µm between frames. Scale bar: 5 µm. **(F)** Scatter dot plots
925 representing growth rate (*top*, *left*), shrinkage rate (*top*, *right*), catastrophe frequency (*bottom*, *left*)
926 and MT dynamicity (*bottom*, *right*) in Homeo, Pro-inf and Anti-inf microglia. Values are
927 expressed as mean ± SEM (Homeo n = 30, Pro-inf n = 27 and Anti-inf n = 29 cells from 4
928 independent experiments). *** p <0.001; ** p <0.01; * p <0.05. One-way ANOVA - Dunnett's
929 multiple comparison test.
930
931 **Fig. 2. Homeostatic, pro-inflammatory and anti-inflammatory primary microglia differ in**
932 **MT orientation. (A)** Representative immunofluorescence images of EB1(magenta) and
933 tyrosinated α-tubulin (Tyr tub) (green) in homeostatic (Homeo), pro-inflammatory (Pro-inf) and
934 anti-inflammatory (Anti-inf) microglia. (Scale bar: 20 µm; zoom: 5 µm. Hoechst for nuclei
935 visualization, blue). Cell outlines are indicated by white dashed line. **(B)** Representative inverted
936 contrast single plane image of EB1 immunofluorescence (*top*, *left*. Scale bar 10 µm). Direction of
937 EB1 signal gradient relative to the cell nucleus was used to identify EB1 anterograde (a, red arrow)
938 and retrograde (b, blue arrow) comets (*top*, *right*; scale bar: 2 µm). Bottom: intensity profile of
939 anterograde (left) and retrograde (right) comets. **(C)** Representative z-projection confocal images
940 showing CAMSAP2 (magenta) and Tyr tub (Green) signal in Homeo, Pro-inf and Anti-inf
941 microglia. Cell outlines are indicated by white dashed line (scale bar: 20 µm; zoom: 5 µm. Hoechst
942 for nuclei visualization, blue). **(D)** Single confocal planes at higher magnification of CAMSAP2
943 (magenta) and Tyr tub (Green) signal in Homeo, Pro-inf and Anti-inf microglia. Scale bar: 5 µm.
944 Note that CAMSAP2 signal is present in microglia processes in Homeo and Anti-inf cells. **(E)** Plot
945 showing maximum fluorescence intensity values of CAMSAP2 vs the radial distance from cell
946 nucleus, obtained with radial profiling, in Homeo (n = 18 cells, green), Pro-inf (n = 14 cells,
947 magenta) and Anti-inf (n = 19 cells, blue) microglia. Curve fit was performed using single

948 exponential decay function. Insert: bar chart reporting the exponential decay constant values (K)
949 for each condition (values are expressed as mean ± SEM from 4 independent experiments; *** p
950 <0.001, ** p <0.01 One-way ANOVA – Tukey's multiple comparison test.
951
952 **Fig. 3. Homeostatic microglia nucleate non-centrosomal MTs from Golgi outposts. (A)**
953 Representative images of homeostatic (Homeo), pro-inflammatory (Pro-inf) and anti-
954 inflammatory (Anti-inf) microglia stained for tyrosinated α-tubulin (Tyr tub, green) and γ-tubulin
955 (γ tub, magenta; scale bar: 20 µm; zoom: 5 µm. Hoechst for nuclei visualization, blue). **(B)** Plot
956 showing maximum fluorescence intensity values of γ tub vs the radial distance from cell nucleus,
957 obtained with radial profiling, in Homeo (n = 13 cells, green), Pro-inf (n = 14 cells, magenta) and
958 Anti-inf (n = 14 cells, blue) microglia. Curve fit was performed using single exponential decay
959 function. Insert: bar chart reporting the exponential decay constant values (K) for each condition
960 (values are expressed as mean ± SEM from 3 independent experiments; *** p <0.001, One-way
961 ANOVA – Tukey's multiple comparison). Note faster decay of γ-tub signal in Pro-inf microglia.
962 **(C)** Representative confocal images showing co-staining of tyrosinated tubulin (Tyr tub) (green)
963 and GM130 (magenta) in Homeo, Pro-inf and Anti-inf microglia (scale bar: 20 µm; zoom: 5 µm.
964 Hoechst for nuclei visualization, blue). **(D)** Violin plot showing number of isolated Golgi stacks
965 per cell in the three phenotypes. Values are expressed as mean ± SEM of Homeo n = 57, Pro-inf n
966 = 34 and Anti-inf n = 36 cells from 3 independent experiments. ** p <0.01. Kuskall-Wallis -
967 Dunn's multiple comparison test. **(E)** Representative images showing GM130 (cyan) and γ-tub
968 (magenta) staining in Homeo microglia. (Scale bar: 20 µm; zoom: 2 µm. Hoechst for nuclei
969 visualization, blue). Note the presence of Golgi outposts in microglia processes. **(F)** Representative
970 confocal images of the time course of the MT re-nucleation assay after nocodazole washout in
971 Homeo microglia stained for Tyr tub (green), GM130 (gray) and γ tub (magenta). Scale bar: 20
972 µm; zoom: 5 µm. Hoechst for nuclei visualization, blue). Time 0' represents the MT
973 depolymerizing effect of nocodazole in homeostatic cells without free tubulin extraction. Note that
974 MTs nucleate from distal Golgi outposts that are positive for γ-tubulin. **(G)** Representative z-
975 projection confocal images of retinal slices (50 µm thickness) from cx3cr1$^{gfp/+}$ mice, expressing
976 GFP in microglia cells, stained with GM130 (magenta) to visualize Golgi outposts. Scale bar: 5
977 µm. Zoom is a single confocal plane of a microglia ramification stained for GM130; scale bar: 5
978 µm.
979

980 **Fig 4. Redistribution of pericentriolar material is a hallmark of pro-inflammatory microglia**
981 ***in vitro* and *in vivo*. (A)** Representative confocal images showing γ-tubulin (γ tub) puncta
982 (magenta) and tyrosinated α-tubulin (Tyr Tub, green) immunolabeling in pro-inflammatory (Pro-
983 inf) microglia (*left*, *middle*). Scale bar: 5 µm. Hoechst for nuclei visualization, blue. *Right:* relative
984 volume view *(top)* and 3D rendering *(bottom)* of γ tub puncta (magenta) acquired via structured
985 illumination microscopy. **(B)** Bar chart reporting the percentage of cells displaying 1-2 γ tub puncta
986 (white bars) or >3 γ tub puncta (black bars) in homestatic (Homeo), pro-inflammatory (Pro-inf)
987 and anti-inflammatory (Anti-inf) microglia. Values are expressed as mean ± SEM from 3
988 independent experiments. ** $p < 0.01$. One-way ANOVA - Dunnett's multiple comparison test.
989 **(C)** Time course of γ -tubulin (γ tub) redistribution during the process of microglia pro-
990 inflammatory activation: representative images showing γ tub (magenta) and tyrosinated α -
991 tubulin (Tyr tub, green) staining at different time points (0 min, 30 min, 2 h, 24 h, 48 h). Scale bar:
992 20 µm; zoom, 2 µm. Hoechst for nuclei visualization, blue. **(D)** Time course of the number of γ
993 puncta per cell (top) and the quantification of γ puncta fluorescence intensity (bottom) during the
994 process of microglia pro-inflammatory activation. Values are expressed as median ± interquartile
995 range (T0 n = 32; T30 min n = 40; T2h n = 44; T24h n = 41; T48h n = 33; from 3 independent
996 experiments); *** $p < 0.001$; ** $p < 0.01$; * $p < 0.05$, Kruskal-Wallis test - Dunn's multiple
997 comparison test respect to T0. **(E)** *Right*: representative maximum intensity projections of retinal
998 slices (50 µm thickness) from control (CTRL) mice stained for γ tub (magenta) and Iba-1 (green)
999 antibodies (Scale bar: 10 µm. Hoechst for nuclei visualization, blue). *Left*: 3D rendering of same
1000 retinal microglia highlighting the intracellular distribution of γ tub in CTRL (sham) and LPS
1001 treated mice. Scale bar: 10 µm. **(F)** *Left*: scatter dot plot showing the γ tub signal over the cell area
1002 of retinal microglia from CTRL (sham) and LPS treated mice. Values are expressed as mean ±
1003 SEM of n = 11/3 cells/mice (CTRL) and n = 9/3 cells/mice (LPS). * $p < 0.05$. Student's t-test.
1004 *Right*: violin plot showing the number of γ tub puncta per microglia in retinal slices from CTRL
1005 and LPS treated mice of n = 28/3 cells/mice (CTRL) and n = 26/3 cells/mice (LPS). *** $p < 0.001$,
1006 Student's t-test.
1007
1008 **Fig 5. Inhibition of pericentriolar material maturation induces NLRP3 inflammasome**
1009 **hyperactivation in pro-inflammatory microglia**
1010 **(A)** Experimental timeline of PLK4 inhibitor treatment and pro-inflammatory cytokine
1011 administration. **(B)** Scanning electron micrographs showing extracellular vesicles (EVs) on the

1012 surface of LPS-IFNγ (*left*) and PLK4 inhibitor+LPS-IFNγ (*right*). Scale bar: 10 µm. **(C)** *Top*:
1013 violin plot showing the number of EVs in Pro-inf microglia with or without PLK4inh treatment
1014 (LPS-IFNγ n = 17 cells, PLK4 inhibitor+LPS-IFNγ n = 19 cells from 2 independent cultures; ***
1015 p <0.001, Student's t-test). *Bottom*: distribution of EV size measured on cell surface of LPS-IFNγ
1016 and PLK4 inhibitor+LPS-IFNγ microglia (LPS-IFNγ n = 17 cells, PLK4 inhibitor+LPS-IFNγ n =
1017 19 cells). **(D)** *Bottom*: bar chart reporting the amount of NLRP3 protein level in Vehicle, PLK4
1018 inhibitor, LPS-IFNγ and PLK4 inhibitor+LPS-IFNγ microglia; *top*: representative immunoblot of
1019 NLRP3. Values are expressed as median ± interquartile range from 4 independent experiments, *
1020 p <0.05, Mann Whitney test. **(E)** Scatter dot plot showing protein quantification by ELISA of *left*:
1021 IL1β (n = 4 independent experiments, n.d. = non detectable), *middle*: IL-10 (Vehicle n = 3,
1022 PLK4inh n = 3, LPS-IFNγ n = 5 and PLK4 inhibitor+LPS-IFNγ n = 5 independent experiments)
1023 and *right*: IL-6 (n = 4 independent experiments). Values are expressed as mean ± SEM. For IL-
1024 1β: ** p <0.01, Student's t-test. Note that supernatants from both Vehicle and PLK4 inhibitor
1025 microglia have undetectable levels of cytokine. For IL-10 and IL-6: *** p <0.001, ** p <0.01;
1026 One-way ANOVA - Holm-Šídák's multiple comparison test.

1027

Fig.1

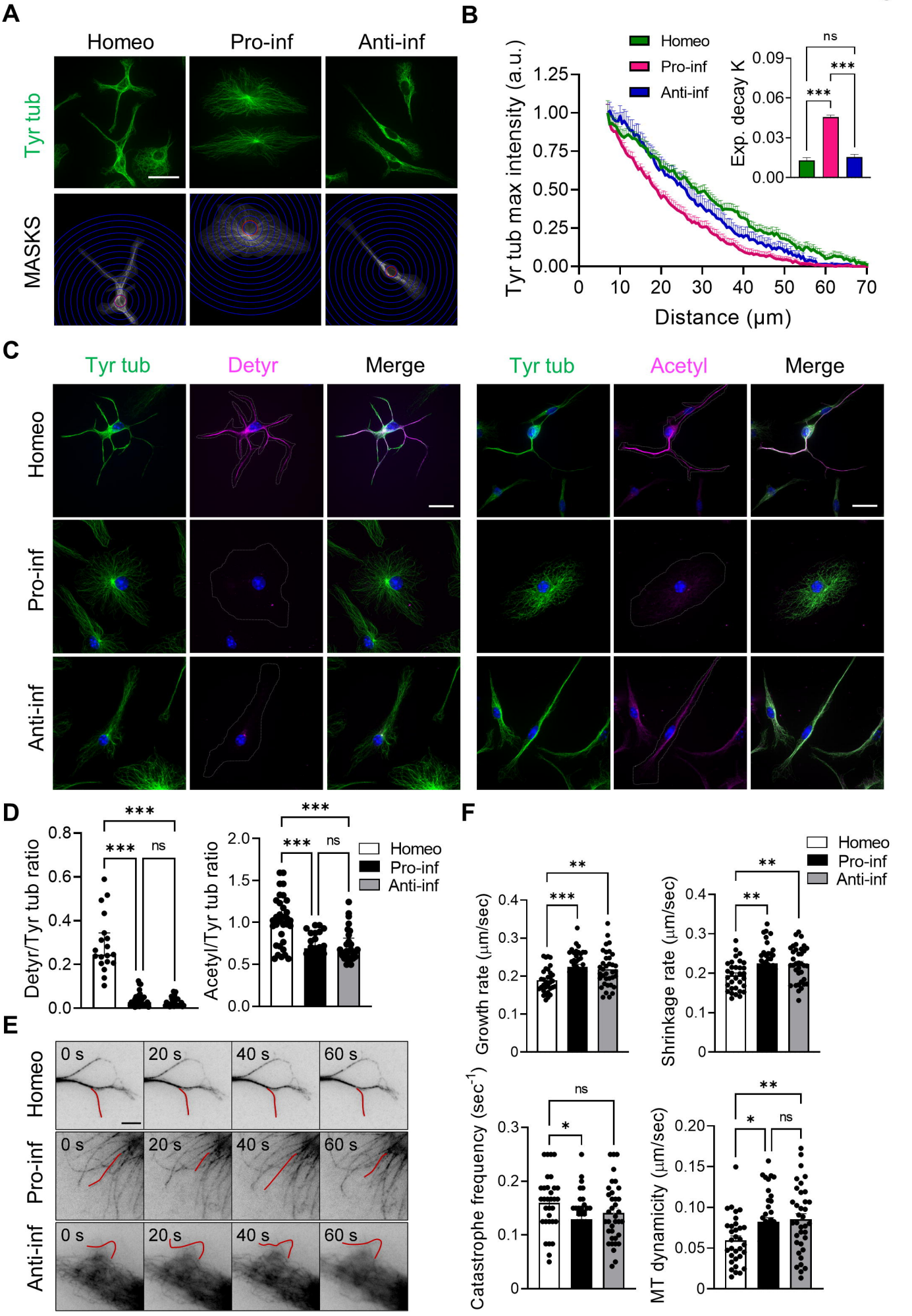
A
Homeo
Pro-inf
Anti-inf
Tyr tub
MASKS
B
Homeo
Pro-inf
Anti-inf
Tyr tub max intensity (a.u.)
Distance (µm)
Exp. decay K
ns
***
***
C
Tyr tub
Detyr
Merge
Tyr tub
Acetyl
Merge
Homeo
Pro-inf
Anti-inf
D
Detyr/Tyr tub ratio
Acetyl/Tyr tub ratio
***
***
ns
Homeo
Pro-inf
Anti-inf
E
0 s
20 s
40 s
60 s
Homeo
Pro-inf
Anti-inf
F
Homeo
Pro-inf
Anti-inf
Growth rate (µm/sec)
Shrinkage rate (µm/sec)
Catastrophe frequency (sec-1)
MT dynamicity (µm/sec)
**
***
ns
*

Fig.2

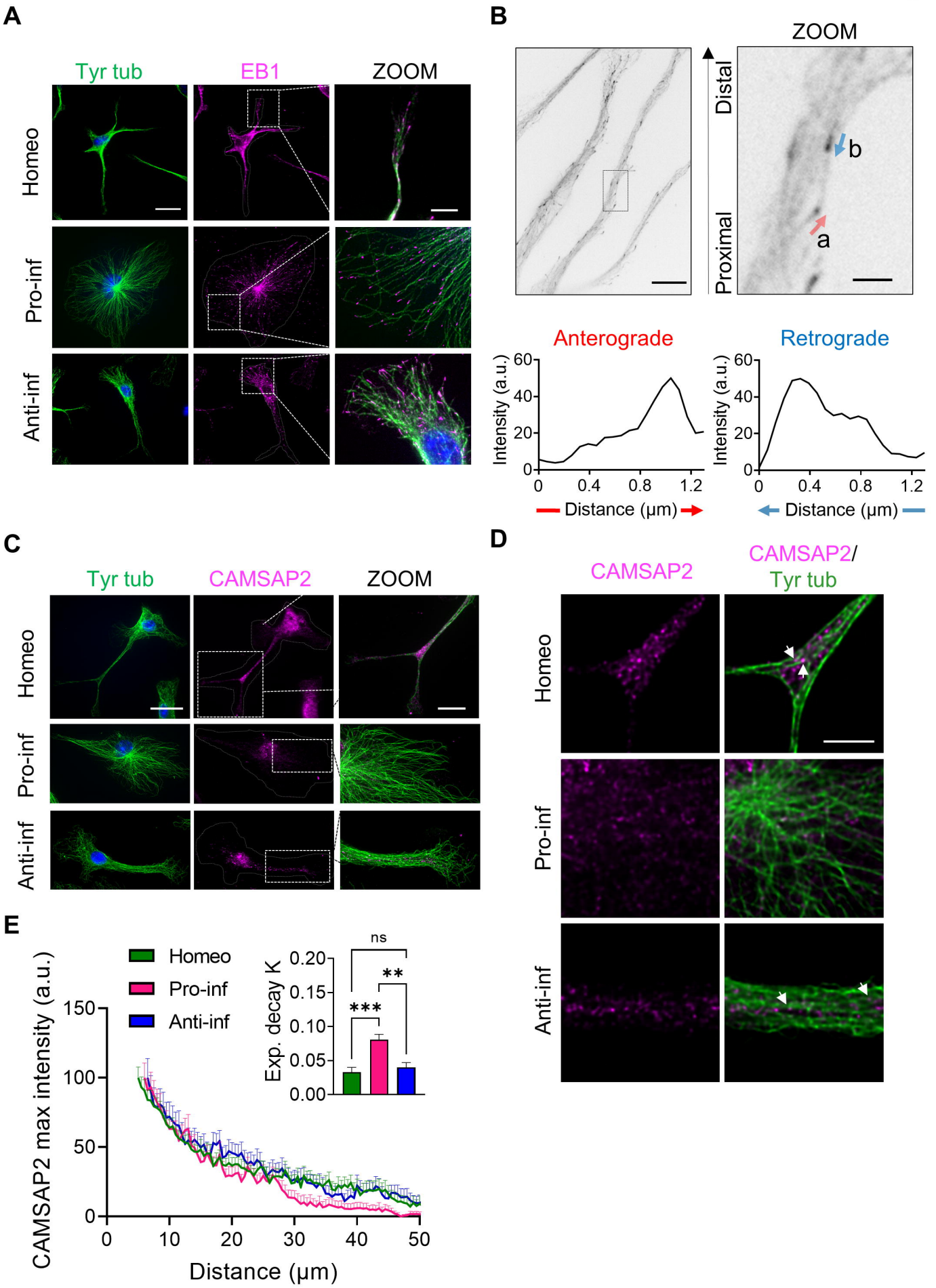
A
Tyr tub
EB1
ZOOM
Homeo
Pro-inf
Anti-inf
B
ZOOM
Distal
Proximal
b
a
Anterograde
Retrograde
Intensity (a.u.)
Distance (μm)
C
Tyr tub
CAMSAP2
ZOOM
Homeo
Pro-inf
Anti-inf
D
CAMSAP2
CAMSAP2/
Tyr tub
Homeo
Pro-inf
Anti-inf
E
Homeo
Pro-inf
Anti-inf
CAMSAP2 max intensity (a.u.)
Distance (μm)
Exp. decay K
ns
**
***

Fig.3

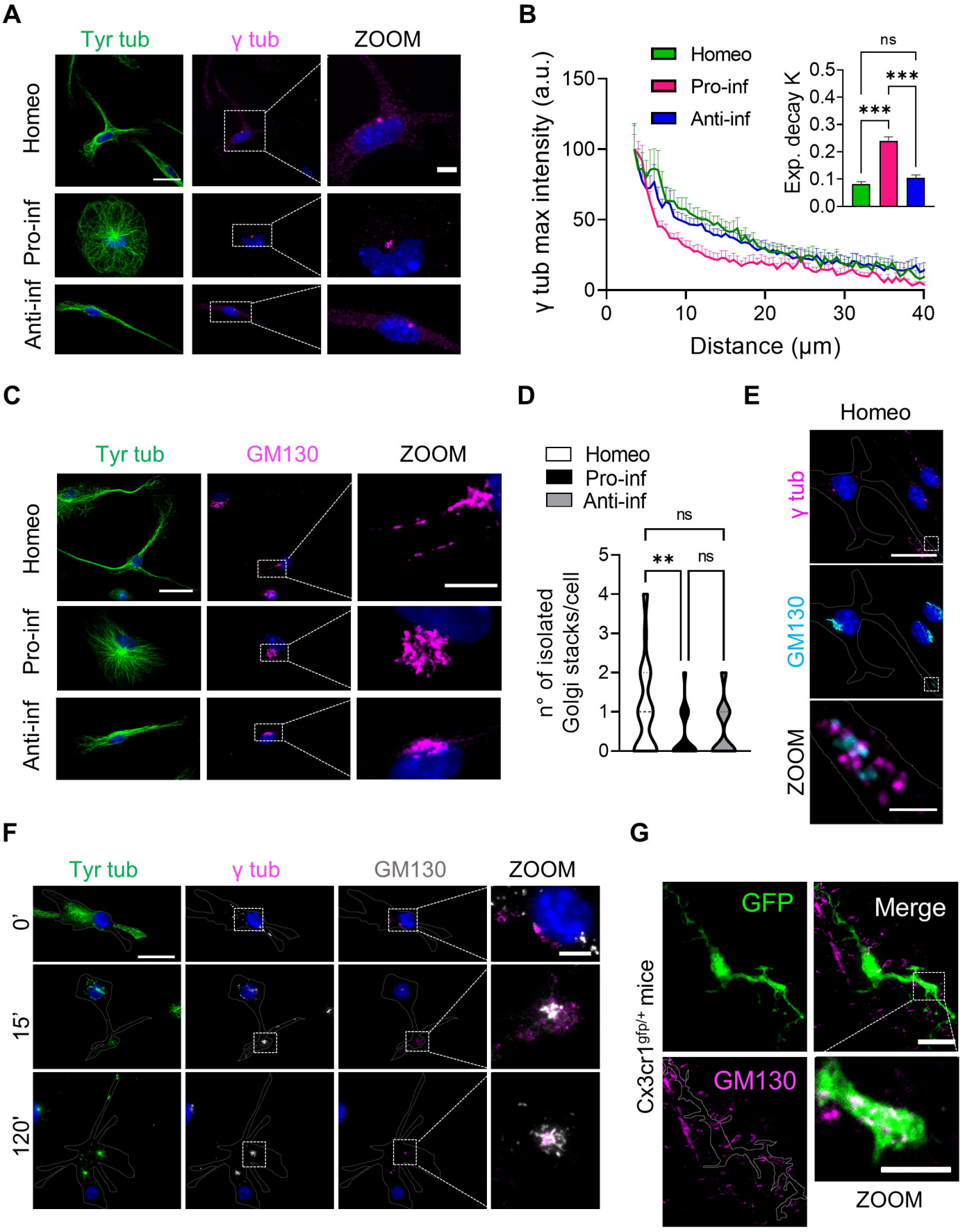
A
Tyr tub
γ tub
ZOOM
Homeo
Pro-inf
Anti-inf
B
Homeo
Pro-inf
Anti-inf
γ tub max intensity (a.u.)
150
100
50
0
0
10
20
30
40
Distance (µm)
Exp. decay K
0.5
0.4
0.3
0.2
0.1
0.0
ns
***
***
C
Tyr tub
GM130
ZOOM
Homeo
Pro-inf
Anti-inf
D
Homeo
Pro-inf
Anti-inf
n° of isolated Golgi stacks/cell
5
4
3
2
1
0
ns
**
ns
E
Homeo
γ tub
GM130
ZOOM
F
Tyr tub
γ tub
GM130
ZOOM
0'
15'
120'
G
GFP
Merge
GM130
ZOOM
Cx3cr1gfp/+ mice

Fig.4

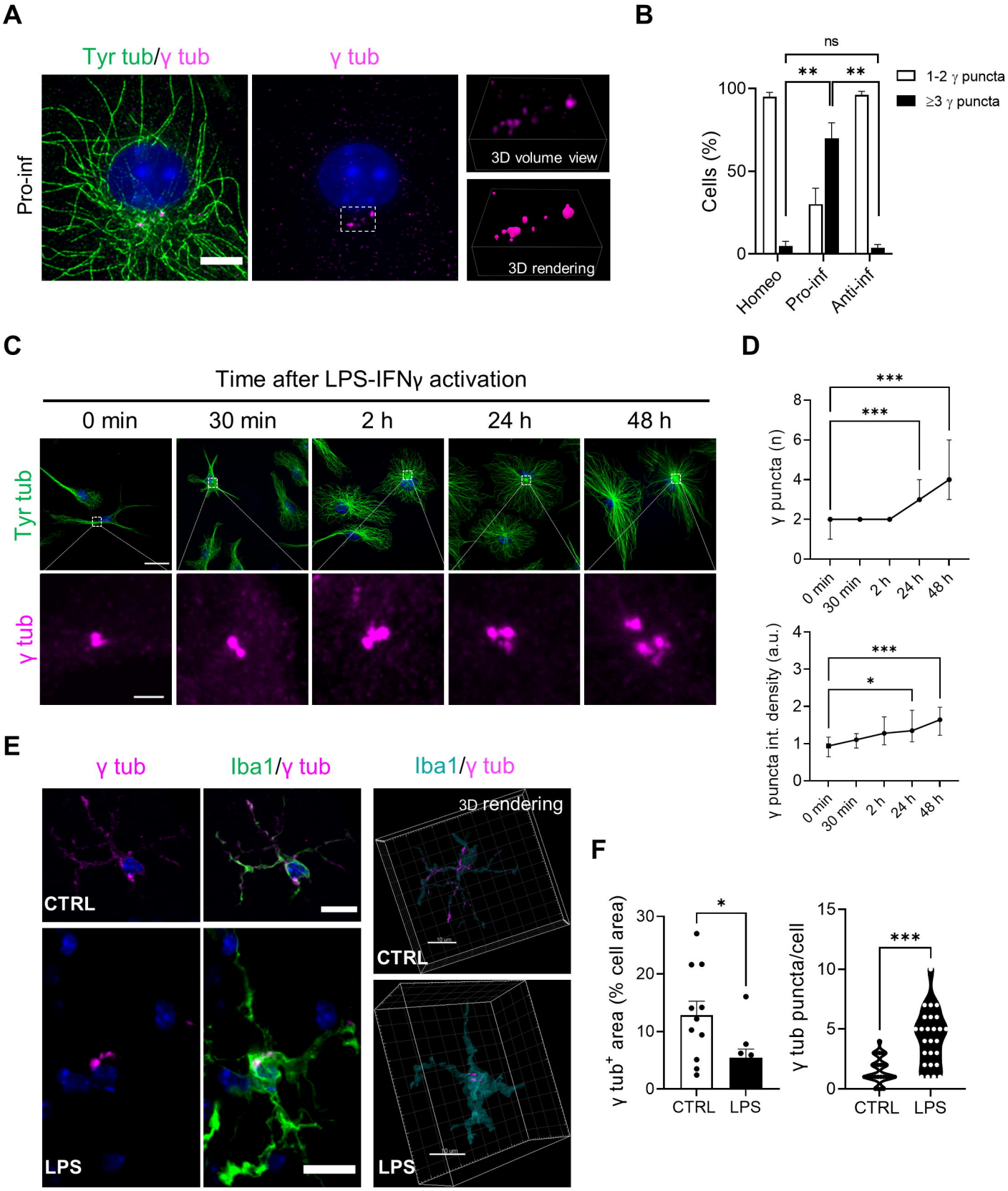
A
Tyr tub/γ tub
γ tub
Pro-inf
3D volume view
3D rendering
B
ns
**
**
1-2 γ puncta
≥3 γ puncta
Cells (%)
100
50
0
Homeo
Pro-inf
Anti-inf
C
Time after LPS-IFNγ activation
0 min
30 min
2 h
24 h
48 h
Tyr tub
γ tub
D
***
***
γ puncta (n)
8
6
4
2
0
0 min
30 min
2 h
24 h
48 h
***
*
γ puncta int. density (a.u.)
4
3
2
1
0
E
γ tub
Iba1/γ tub
Iba1/γ tub
3D rendering
CTRL
LPS
CTRL
LPS
F
*
γ tub+ area (% cell area)
30
20
10
0
CTRL
LPS
***
γ tub puncta/cell
15
10
5
0
CTRL
LPS

Fig. 5

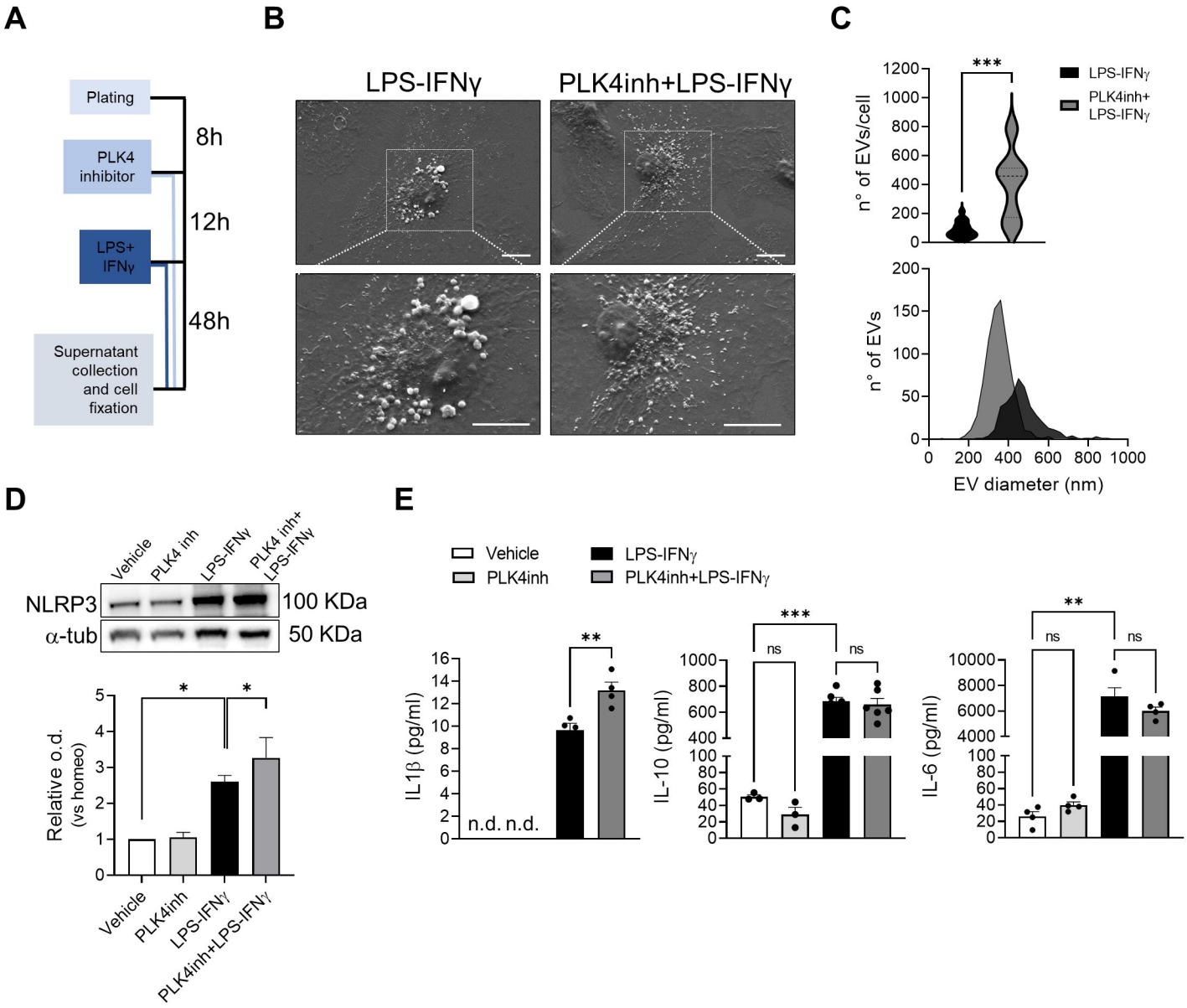
A
Plating
PLK4 inhibitor
LPS+ IFNγ
Supernatant collection and cell fixation
8h
12h
48h
B
LPS-IFNγ
PLK4inh+LPS-IFNγ
C
***
LPS-IFNγ
PLK4inh+ LPS-IFNγ
n° of EVs/cell
n° of EVs
EV diameter (nm)
D
Vehicle
PLK4 inh
LPS-IFNγ
PLK4 inh+ LPS-IFNγ
NLRP3
α-tub
100 KDa
50 KDa
Relative o.d. (vs homeo)
*
*
Vehicle
PLK4inh
LPS-IFNγ
PLK4inh+LPS-IFNγ
E
Vehicle
PLK4inh
LPS-IFNγ
PLK4inh+LPS-IFNγ
IL1β (pg/ml)
n.d. n.d.
**
IL-10 (pg/ml)
***
ns
ns
IL-6 (pg/ml)
**
ns
ns

	Homeo	Pro-inf	Anti-inf
Growth rate (µm/s)	0.19 ± 0.01	0.22 ± 0.01 ***	0.22 ± 0.01 **
Shrinkage rate (µm/s)	0.9 ± 0.01	0.23 ± 0.01 **	0.22 ± 0.01 **
% growth	15 ± 1	20 ± 1 *	18 ± 1
% shrinkage	15 ± 1	16 ± 1	19 ± 1
% pausing	70 ± 2	64 ± 2	63 ± 2
Catastrophe frequency (s^{-1})	0.16 ± 0.01	0.13 ± 0.01 *	0.14 ± 0.01
Rescue frequency (s^{-1})	0.14 ± 0.06	0.15 ± 0.01	0.13 ± 0.01
MT dinamicity (µm/s)	0.06 ± 0.01	0.08 ± 0.01 *	0.09 ± 0.01 **
MTs (n)	32	40	36
Cells (n)	30	27	29

Table 1. MT dynamicity parameters in homeostatic and activated microglia

Table reporting parameters of MT dynamics obtained from wide field fluorescence time lapse analysis of SiRTubulin in homeostatic (Homeo), pro-inflammatory (Pro-inf) and anti-inflammatory (Anti-inf) microglia. Values are expressed as mean ± SEM from Homeo n = 32/30 MTs/cells, Pro-inf n = 40/27 MTs/cells and Anti-inf n = 36/29 MTs/cells arising from 4 independent experiments. *** $p < 0.001$; ** $p < 0.01$; * $p < 0.05$. One-way ANOVA - Dunnett's multiple comparison test.